Syracuse University

SURFACE

2003

Amorphous Silicon Based Solar Cells

Xunming Deng
University of Toledo

Eric A. Schiff
Syracuse University

Follow this and additional works at: https://surface.syr.edu/phy

Part of the Physics Commons

Recommended Citation

12

Amorphous Silicon–based Solar Cells

Xunming Deng[1] and Eric A. Schiff[2]

[1]*University of Toledo, Toledo, OH, USA,* [2]*Syracuse University, Syracuse, NY, USA*

12.1 OVERVIEW

12.1.1 Amorphous Silicon: The First Bipolar Amorphous Semiconductor

Crystalline semiconductors are very well known, including silicon (the basis of the integrated circuits used in modern electronics), Ge (the material of the first transistor), GaAs and the other III-V compounds (the basis for many light emitters), and CdS (often used as a light sensor). In crystals, the atoms are arranged in near-perfect, regular arrays or *lattices*. Of course, the lattice must be consistent with the underlying chemical bonding properties of the atoms. For example, a silicon atom forms four covalent bonds to neighboring atoms arranged symmetrically about it. This "tetrahedral" configuration is perfectly maintained in the "diamond" lattice of crystal silicon.

There are also many *noncrystalline* semiconductors. In these materials the chemical bonding of atoms is nearly unchanged from that of crystals. Nonetheless, a fairly small, disorderly variation in the angles between bonds eliminates the regular lattice structure. Such noncrystalline semiconductors can have fairly good electronic properties – sufficient for many applications. The first commercially important example was xerography [1, 2], which exploited the *photoconductivity* of noncrystalline selenium. As do all semiconductors, selenium absorbs those photons from an incident light beam that have photon energies exceeding some threshold energy. The photon that is absorbed generates a positively charged "hole" and a negatively charged electron that are separated and swept away by the large electric fields used in xerography.

However, solar cells require that photogenerated electrons and holes be separated by relatively modest electric fields that are "built-in" to the device, and selenium and many other noncrystalline semiconductors proved unsuitable for making efficient cells.

In Dundee, Scotland, Walter Spear and Peter LeComber discovered around 1973 that amorphous silicon prepared using a "glow discharge" in silane (SiH_4) gas had unusually good electronic properties; they were building on earlier work by Chittick, Sterling, and Alexander [3]. Glow discharges are the basis for the familiar "neon" light; under certain conditions, an electric voltage applied across a gas can induce a significant electrical current through the gas, and the molecules of the gas often emit light when excited by the current. Amorphous silicon was deposited as a thin film on substrates inserted into the silane gas discharge.[1] Spear and LeComber reported in 1975 [4] that amorphous silicon's conductivity could be increased enormously either by mixing some phosphine (PH_3) gas or some diborane (B_2H_6) gas with the silane. Just as for crystal silicon, the phosphorus doping of the amorphous silicon had induced a conductivity associated with mobile electrons (the material was "*n*-type"), and the boron doping had induced a conductivity associated with mobile holes (the material was "*p*-type").

In 1974, at the Radio Corporation of America (RCA) Research Laboratory in Princeton, David Carlson discovered that he could make fairly efficient solar cells using a silane glow discharge to deposit films. In 1976, he and Christopher Wronski reported a solar cell based on amorphous silicon [5] with a solar conversion efficiency of about 2.4% (for historical discussion see Reference [6, 7]).

Carlson and Wronski's report of the current density versus output voltage is presented in Figure 12.1 (along with the curve from a far more efficient cell reported in 1997 [8]). As these scientists had discovered, the optoelectronic properties of amorphous silicon made by glow discharge (or "plasma deposition") are very much superior to the amorphous silicon thin films prepared, for example, by simply evaporating silicon.
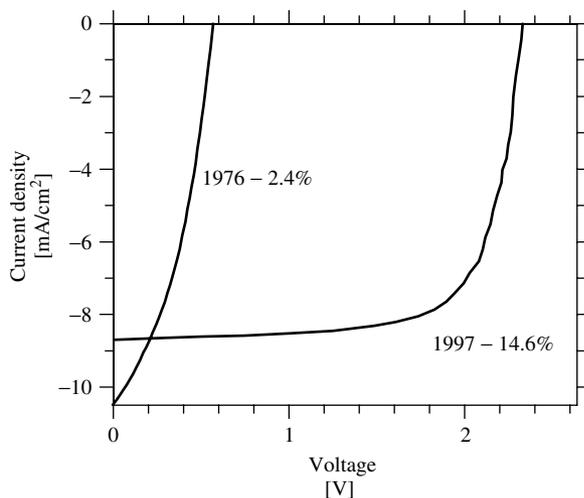

Figure 12.1   Current density versus voltage under solar illumination for a very early single-junction amorphous silicon solar cell (Carlson and Wronski [5]) and from a recent "triple-junction" cell (Yang, Banerjee, and Guha [8]). The stabilized efficiency of the triple-junction cell is 13.0%; the active area is 0.25 cm^2

---

[1] The term *amorphous* is commonly applied to noncrystalline materials prepared by deposition from gases.

After several years of uncertainty, it emerged that plasma-deposited amorphous silicon contained a significant percentage of hydrogen atoms bonded into the amorphous silicon structure and that these hydrogen atoms were essential to the improvement of the electronic properties of the plasma-deposited material [9]. As a consequence, the improved form of amorphous silicon has generally been known as *hydrogenated amorphous silicon* (or, more briefly, a-Si:H). In recent years, many authors have used the term *amorphous silicon* to refer to the hydrogenated form, which acknowledges that the unhydrogenated forms of amorphous silicon are only infrequently studied today.

Why was there so much excitement about the amorphous silicon solar cells fabricated by Carlson and Wronski? First, the technology involved is relatively simple and inexpensive compared to the technologies for growing crystals. Additionally, the optical properties of amorphous silicon are very promising for collecting solar energy, as we now explain. In Figure 12.2, the upper panel shows the spectrum for the optical absorption coefficients $\alpha(h\nu)$ for amorphous silicon and for crystalline silicon [10].[2] In the lower panel of the figure, we show the spectrum of the "integrated solar irradiance;" this is the intensity (in W/m^2) of the solar energy carried by photons above an energy threshold $h\nu$ [11].
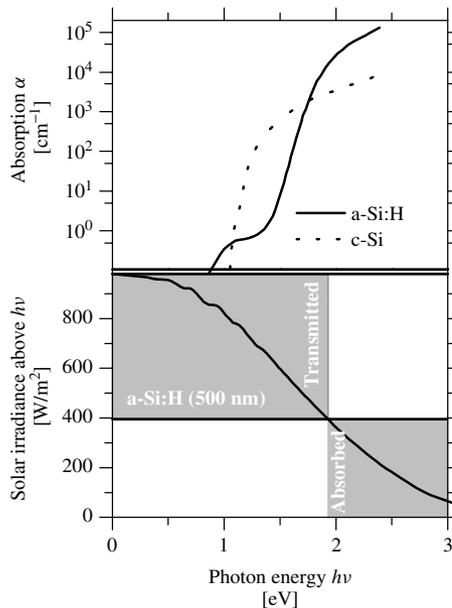

Figure 12.2 (Upper panel) Spectra of the optical absorption coefficient $\alpha(h\nu)$ as a function of photon energy $h\nu$ for crystalline silicon (c-Si) and for hydrogenated amorphous silicon (a-Si:H). (Lower panel) The solid curve indicates the irradiance of photons in the solar spectrum with energies $h\nu$ or larger. An a-Si:H film that is 500 nm thick mostly absorbs photons above 1.9 eV; as indicated by the shaded areas, this corresponds to an absorbed irradiance of about 390 W/m^2. After Vaněček M *et al.*, *J. Non-Cryst. Solids* **227–230**, 967 (1998) [10]

[2] We assume familiarity with the concept of a photon energy $h\nu$ and of an optical absorption coefficient α; see Chapter 3.

We use these spectra to find out how much solar energy is absorbed by layers of varying thickness. The example used in the figure is an a-Si:H layer with a thickness $d = 500$ nm. Such a layer absorbs essentially all photons with energies greater than 1.9 eV (the energy at which $\alpha = 1/d$). We then look up how much solar irradiance lies above 1.9 eV. Assuming that the reflection of sunlight has been minimized, we find that about 420 W/m^2 is absorbed by the layer (the gray area labeled "absorbed"). Through such a layer 580 W/m^2 of energy is transmitted. These energies may be compared to the results for c-Si, for which a 500-nm-thick layer absorbs less than 200 W/m^2.

To absorb the same energy as the 500-nm a-Si:H layer, a c-Si layer needs to be much thicker. The implication is that much less material is required to make a solar cell from a-Si than from c-Si.[3] In the remainder of this section, we first describe how amorphous silicon solar cells are realized in practice, and we then briefly summarize some important aspects of their electrical characteristics.

12.1.2 Designs for Amorphous Silicon Solar Cells: A Guided Tour

Figure 12.1 illustrates the tremendous progress over the last 25 years in improving the efficiency of amorphous silicon–based solar cells. In this section we briefly introduce three basic ideas involved in contemporary, high-efficiency devices: (1) the *pin* photodiode structure, (2) the distinction between "substrate" and "superstrate" optical designs, and (3) multijunction photodiode structures. A good deal of this chapter is devoted to more detailed reviews of the implementation and importance of these concepts.

12.1.2.1 pin photodiodes

The fundamental photodiode inside an amorphous silicon–based solar cell has three layers deposited in either the *p-i-n* or the *n-i-p* sequence. The three layers are a very thin (typically 20 nm) *p*-type layer, a much thicker (typically a few hundred nanometer), undoped *intrinsic* (*i*) layer, and a very thin *n*-type layer. As illustrated in Figure 12.3, in this structure excess electrons are actually donated from the *n*-type layer to the *p*-type layer, leaving the layers positively and negatively charged (respectively), and creating a sizable "built-in" electric field (typically more than 10^4 V/cm).

Sunlight enters the photodiode as a stream of photons that pass through the *p*-type layer, which is a nearly transparent "window" layer. The solar photons are mostly absorbed in the much thicker intrinsic layer; each photon that is absorbed will generate one electron and one hole photocarrier [12, 13]. The photocarriers are swept away by the built-in electric field to the *n*-type and *p*-type layers, respectively – thus generating solar electricity!

The use of a *pin* structure for a-Si:H-based solar cells is something of a departure from solar cell designs for other materials, which are often based on simpler *p-n* structures.

---

[3] The very different optical properties of c-Si and a-Si reflect the completely different nature of their electronic states. In solid-state physics textbooks, one learns about the "selection rules" that greatly reduce optical absorption in c-Si, which is an "indirect band gap" semiconductor. Such selections rules do not apply to a-Si. Additionally, the "band gap" of a-Si is considerably larger than that for c-Si.
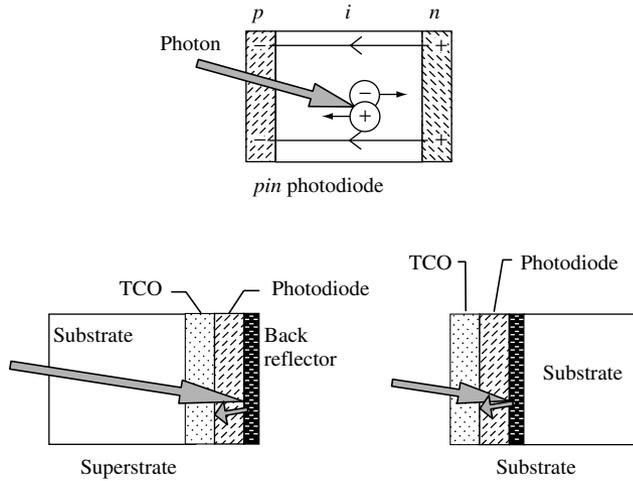
Figure 12.3   In a *pin* photodiode, excess electrons are donated from the *n*-type to the *p*-type layers, leaving the charges and electric fields illustrated. Each photon absorbed in the undoped, intrinsic layer generates an electron and a hole photocarrier. The electric field causes these carriers to drift in the directions shown. *pin* diodes are incorporated into solar cells in either the superstrate or substrate designs. For amorphous silicon–based cells, photons invariably enter through the *p*-type window layer as shown here

For doped a-Si:H, it turns out that minority photocarriers (holes in *n*-type a-Si:H, electrons in *p*-type a-Si:H) do not move very far, and so a *p-n* structure would only collect photocarriers from photons generated in an extremely thin layer of doped a-Si:H. Indeed, in analyzing the performance of a-Si:H-based solar cells, one normally considers any photons absorbed by the doped layers to be "wasted." The trick of keeping the doping atoms out of the absorber layer enables this layer to be thick enough to capture most of the sunlight.

In Section 12.4 you will find a more detailed description of the device physics of the *pin* solar cell; the description explains why the window layer is the *p*-type one, and also explains the design trade-offs that determine the thickness of the absorber layer.

12.1.2.2 Substrate and superstrate designs

One of the advantages of amorphous silicon–based solar cells is that they absorb sunlight very efficiently: the total thickness of the absorbing layers in amorphous silicon solar cells is less than 1 μm. Consequently, these layers need to be supported on a much thicker substrate. Two totally different designs for amorphous silicon solar cells have evolved corresponding to transparent and opaque substrates. We have illustrated the two designs in Figure 12.3.

In the "superstrate" design, sunlight enters through the transparent substrate, which is usually glass or a transparent plastic. The insulating substrate needs a conducting layer, which is typically a "transparent conductive oxide" (TCO) such as SnO_2. The amorphous silicon photodiode layers are then deposited onto the TCO, starting with a *p*-type window

layer. Finally, a "back" reflector is deposited onto the photodiode; the back reflector acts as an electrode to the *n*-type photodiode layer.

In the "substrate" design, sunlight enters the photodiode before it reaches the substrate. Starting with the substrate, the cell is fabricated in the reverse order compared to the superstrate design: first a back reflector, then the photodiode layers (starting with an *n*-type layer), and finally a TCO layer to act as an electrode to the topmost, window layer of the photodiode.

These two designs permit a very wide range of applications for amorphous silicon solar cells. The superstrate design (light enters through the substrate) is particularly suited to building-integrated solar cells in which a glass substrate can be used as an architectural element. The substrate design has generally been applied to solar cells using flexible, stainless steel (SS) substrates. The detailed construction of a deposition facility of course depends upon whether the substrate is rigid or flexible. Finally, it turns out that there is a profound effect of the substrate upon the properties of the first photodiode layers deposited upon it; this effect has led to fairly different photodiode structures for the superstrate and substrate designs.

12.1.2.3 Multijunction solar cells

The conversion efficiency of the relatively simple, amorphous silicon *pin* photodiode structure just described can be significantly improved by depositing two or three such photodiodes, one on top of another, to create a "multijunction" device. We illustrate a "tandem" device in Figure 12.4, which shows a combination of two *pin* diodes.[4] Note that the "bottom" cell is not based on a-Si:H, but rather upon an amorphous silicon–germanium alloy made by including germane (GeH_4) gas in the plasma-deposition recipe.

The main advantage of the tandem design over the simpler single-junction one is due to "spectrum splitting" of the solar illumination. Since the absorption coefficient of light rises rapidly with the photon energy, the topmost layer of a tandem cell acts
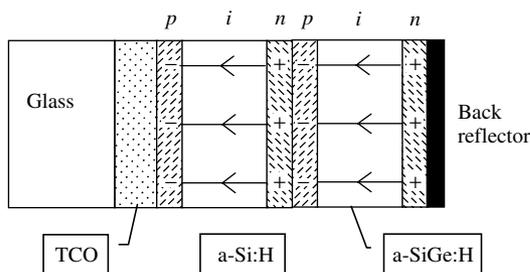

Figure 12.4 A multijunction solar cell consisting of two *pin* solar cells deposited in series. Double-junction (or "tandem," as shown) and triple-junction designs can be significantly more efficient than single-junction designs. Substrate texturing, which is important in real devices, is not indicated; see Section 12.4.5

---

[4] It is worth noting that the adjoining *p*-type and *n*-type layers do *not* form a *p-n* junction diode, but rather a simple Ohmic contact. We discuss the interesting physics underlying this fact in Section 12.5.3.

as a "low-pass" optical filter. This effect is illustrated in Figure 12.2, which shows that a 0.5-μm layer of a-Si:H absorbs photons with energies larger than 1.9 eV and passes photons with smaller energies. The "wasted" lower energy photons can be efficiently harvested by amorphous silicon-germanium, which has a much larger optical absorption coefficient below 1.9 eV than does a-Si:H, hence a lower threshold energy. Overall, the advantages of the multijunction design are sufficiently compelling that they usually overcome the additional complexity and cost of the deposition facility. Both tandem and triple-junction devices are being manufactured today. We discuss multijunction solar cells in detail in Section 12.5.

12.1.3 Staebler–Wronski Effect

One of the most intriguing and actively researched facets of amorphous silicon solar cells is the significant decline in their efficiency during their first few hundred hours of illumination. Figure 12.5 illustrates this effect for a single-junction cell and for a triple-junction module made at United Solar Systems Corp. [14, 15]. The single-junction cell loses about 30% of its initial efficiency after about 1000 h; the triple-junction module loses about 15% of its initial efficiency.

All amorphous silicon–based solar cells exhibit this type of initial behavior under illumination; the behavior is mostly due to the "Staebler–Wronski" effect [16], which is the light-induced change in hydrogenated amorphous silicon (a-Si:H) and related materials used in the cell. Although we have not illustrated it here, the Staebler–Wronski effect can be annealed away within a few minutes at temperatures of about 160°C (and the initial performance of the solar cell largely restored).

The Staebler–Wronski effect contributes to noticeable seasonal variations in the conversion efficiency of a-Si:H-based modules in the field. In Figure 12.6 we illustrate

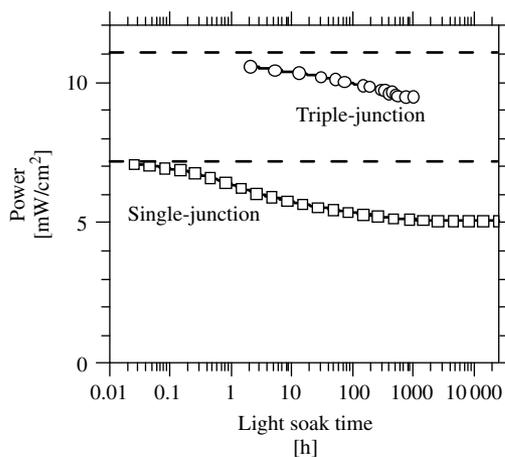**Figure 12.5** The conversion efficiency in a-Si:H-based solar cells declines noticeably upon the first exposure to sunlight. The figure illustrates this decline under a solar simulator (100 mW/cm^2) for a single-junction cell (260-nm i-layer thickness) and for a triple-junction module made at United Solar Systems Corp. [14, 15]; the dashed lines indicate the initial power measured for each device
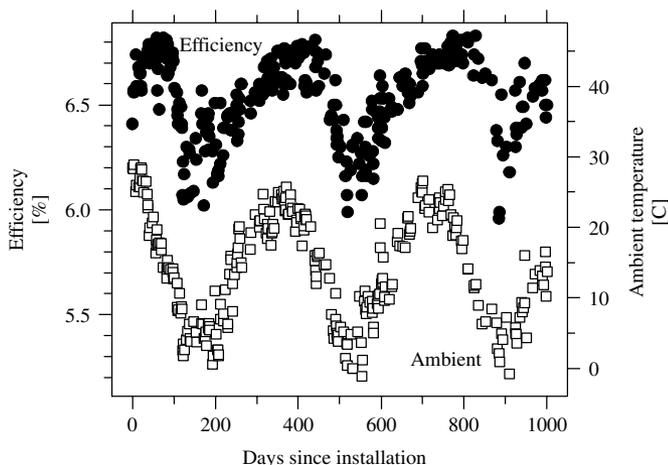
Figure 12.6   Seasonal variations in the average conversion efficiency (solid symbols) of an amorphous silicon triple-junction module [18], along with the daily mean temperature (open symbols)

the daily average conversion efficiency and ambient temperature of a triple-junction module installation in Switzerland. The module performed best in hot weather. Up to 20°C, the relative increase in efficiency with temperature is about $+5 \times 10^{-3}$/K. It is noteworthy that there was no permanent degradation of this module over the three-year extent of the test. The conclusion that amorphous silicon modules reach a steady state after about 1000 h of steady illumination was also reached in a much larger study of modules manufactured by Advanced Photovoltaics Systems, Inc. [17].

This positive trend of efficiency with temperature is atypical of solar cells made with other materials; for example, the temperature coefficient of crystal silicon solar cells is about -4×10^{-3}/K [19, 20]. Interestingly, if the temperature dependence of a-Si:H solar cells is measured quickly – so that there is no time for the Staebler–Wronski effect to set in – the temperature coefficient is also negative (about -1×10^{-3}/K) [19]. The behavior of a module in the field may be understood as a competition of the slow annealing of the Staebler–Wronski effect (which yields the positive temperature coefficient) and of a smaller, intrinsic negative coefficient [21, 22]. The effects of temperature on solar cell performance are discussed in more detail in Chapters 3 and 16.

12.1.4 Synopsis of this Chapter

The remainder of this chapter is organized as follows. In Section 12.2 we introduce some of the fundamental physical concepts required to interpret the scientific literature about amorphous silicon and related materials (such as amorphous silicon−based alloys and, to a much lesser degree, microcrystalline silicon). Section 12.3 surveys the principal methods such as plasma deposition that are used to make amorphous silicon−based solar cells. Section 12.4 describes how the simplest, single-junction solar cell "works," by which we mean how the photoelectric behavior of the cell is related to the fundamental concepts. High-efficiency solar cells based on amorphous silicon technology are multijunction devices, and in Section 12.5 we discuss how these are made and how their

performance can be understood and optimized. Section 12.6 describes some of the issues involved in manufacturing modules. To conclude this chapter, Section 12.7 presents some of the directions that we consider important for future progress in the field.

There have been several excellent monographs and review chapters on amorphous silicon and amorphous silicon–based solar cells in recent years. In the body of the chapter, we direct the reader to these works where we feel that they may be useful for expanded or complementary discussion.

12.2 ATOMIC AND ELECTRONIC STRUCTURE OF HYDROGENATED AMORPHOUS SILICON

12.2.1 Atomic Structure

Silicon atoms in amorphous silicon largely retain the same basic structure as that of crystal silicon: each silicon atom is connected by covalent bonds to four other silicon atoms arranged as a tetrahedron. This understanding emerges from measurements of the scattering ("diffraction") of X rays by the two materials [23] as well as from theoretical and computational studies of the two materials.

If you build a noncrystalline silicon structure with wooden sticks (to represent covalent bonds) and wooden balls drilled with four small holes for the sticks (to represent the silicon atoms), you will have some trouble in making a noncrystalline structure. To avoid a crystalline structure, you will need to bend the sticks. Quite soon, you will have to give up on the fourth stick on some atom, and you will have created an imperfect noncrystalline structure with a "dangling bond." Your problem is related to tetrahedral bonding: there are too many constraints on the positions of atoms to keep *all* bond lengths and angles reasonably close to the values demanded by silicon's chemistry in any non-crystalline structure. The same conclusion is reached by mathematical and computational methods [24, 25]. Alloys such as As_2Se_3, which easily form noncrystalline glasses by cooling from a liquid, have an average number of bonds per atom of about 2.7 or less.

For hydrogenated amorphous silicon (a-Si:H), silicon–hydrogen bonds resolve this structural problem. Several percent of the silicon atoms make covalent bonds with only three silicon neighbors; the fourth valence electron of the silicon bonds to a hydrogen atom. This crucial hydrogen is essentially invisible to X rays, but is quite evident in nonde-structive measurements (proton magnetic resonance [26] and infrared spectroscopy [27]) as well as destructive testing (secondary ion mass spectroscopy [28] and hydrogen evo-lution during annealing [29]).

There are quite a few distinct atomic configurations for the hydrogen in a-Si:H. The two principal "phases" of hydrogen evidenced by proton magnetic resonance are termed the *dilute* and *clustered* phases [26]. In the dilute phase a particular hydrogen atom is about 1 nm away from any other hydrogen atom; in the clustered phase there are two or more hydrogen atoms in close proximity. A computer calculation of a particular instance of this structure [30] is presented in Figure 12.7(a). The densities of hydrogen in each of the individual phases, as well as the total density of hydrogen, depend upon the conditions under which the material is made.
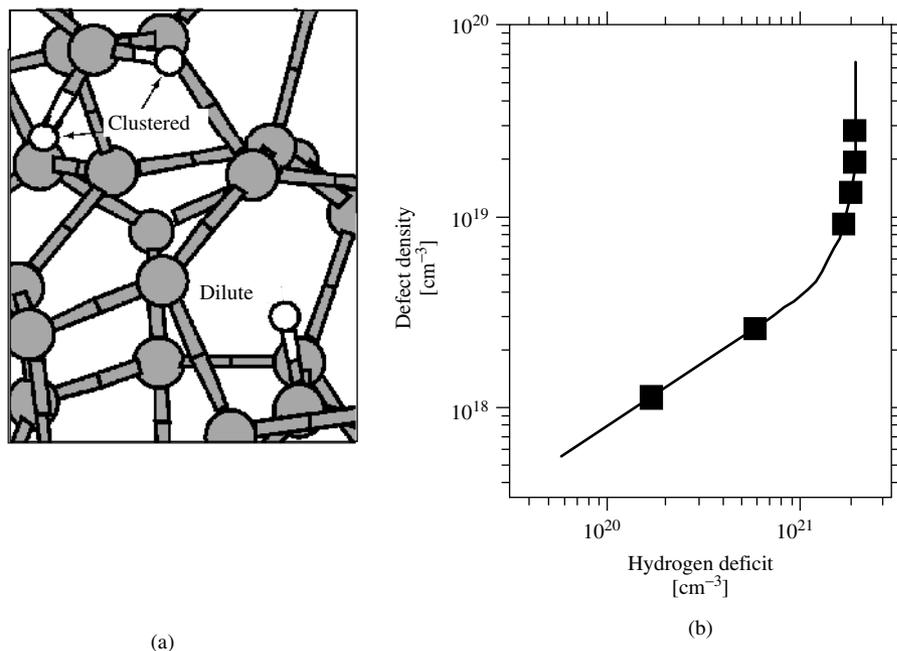
(a)

(b)

Figure 12.7 (a) Computer model of the chemical bonding of hydrogenated amorphous silicon. The larger, gray spheres indicate Si atoms; the smaller, white spheres indicate hydrogen atoms, which are found in clustered and relatively isolated, dilute-phase configurations as indicated. (b) Correlation of the defect (dangling bond) density in a-Si:H with the density of hydrogen removed from the material by heating (the hydrogen deficit). The data points are derived from deuterium and defect profiles by Jackson *et al*. [31] (350°C deuteration). The curve is a fit to a model proposed by Zafar and Schiff [32]

12.2.2 Defects and Metastability

While the underlying structure illustrated in Figure 12.7 is noncrystalline, it is a chemically ideal structure: each atom forms the normal number of chemical bonds (four for silicon, one for hydrogen). This noncrystalline atomic structure largely determines the overall electronic and optical properties of the material, as we will discuss shortly. However, many electronic properties in a-Si:H are also strongly affected by the gross defects of chemical bonding. The atomic structure of the bonding defects in a-Si:H has been extensively studied using electron spin resonance. A single type of defect, the *D*-center, dominates most measurements in undoped a-Si:H [23]. The *D*-center is generally identified as a silicon dangling bond [33].

A dangling bond may be envisioned using Figure 12.7: just imagine that the hydrogen atom is removed from the dilute-phase site in the lower right-hand corner of the figure, leaving behind a single unbonded electron (the "dangling bond"). This simple picture is consistent with the following observation: the density of dangling bonds increases when hydrogen is removed from a-Si:H by heating. We present a comparison of a model for this relationship together with measurements illustrating the effect in Figure 12.7(b) [31, 32]. Note that the density of dangling bonds is generally much lower than the density of
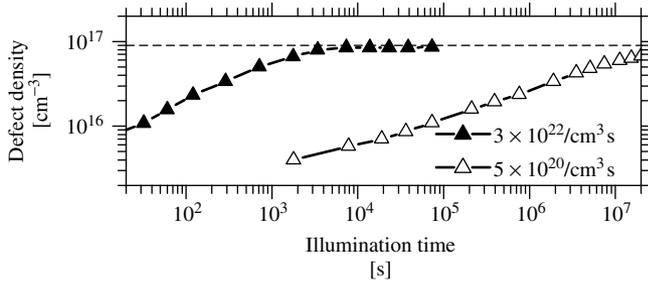
Figure 12.8   Plot of the defect (dangling bond) density during extended illumination of an a-Si:H film as measured by Park, Liu, and Wagner [34]. Data are given for high- and low-intensity illumination; the legend indicates the photocarrier generation rate of each intensity

hydrogen lost from the structure; this effect has been attributed to the evolution of hydrogen from clustered-phase sites, which presumably does not create dangling bonds.

The most intense defect research in a-Si:H has not been focused on the direct hydrogen-defect relation, but rather on the light-soaking effects. We illustrated how light soaking degrades the solar conversion efficiency in Figure 12.5, and in Figure 12.8 we illustrate how it increases the defect density. For the high intensity illumination, the defect density reaches a steady state at about $10^{17}/cm^3$. For purposes of engineering and commercial applications, it is very important that a-Si:H reaches such a "stabilized" condition after extended light soaking.

Although the defect density is not the only property of a-Si:H modified following light soaking [35], most workers believe that the principal cause of the Staebler–Wronski effect is this increase in dangling bond density after light soaking. The close connection between hydrogen and defects in a-Si:H has led to several efforts to understand the defect creation in terms of metastable configurations of hydrogen atoms [35, 36]. The idea is that illumination provides the energy required to shift hydrogen atoms away from their dilute-phase sites, thus creating dangling bonds. The technological importance of establishing the atomic mechanism underlying the Staebler–Wronski effect lies in the possibility that this effect can be mitigated in a-Si:H by changing its preparation conditions.

An essential feature of the light-soaking effects on a-Si:H cells and films is that most of the effects are "metastable" and can be removed nearly completely by annealing of a light-soaked sample at a temperature above 150°C. More generally, the stabilized condition of a-Si:H cells and films is quite temperature-dependent. For example, Figure 12.6 showed that the module efficiency is substantially affected by the seasons and is highest following the hottest days. The measurement may be understood by considering that the stabilized condition is due to competition between two rates: the creation of metastable defects by light and a thermally activated process that anneals them away.

12.2.3 Electronic Density-of-states

The most important concept used in understanding the optical and electronic properties of semiconductors is the electronic density-of-states, $g(E)$. The idea is a simple approximation: if a single electron is added to a solid, it may be viewed as occupying a well-defined
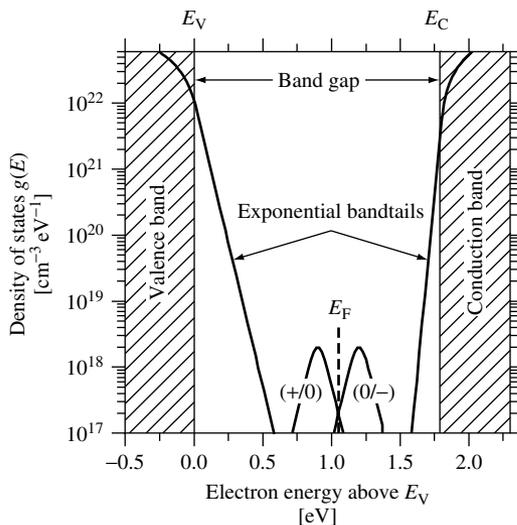
Figure 12.9 Density of electronic states $g(E)$ in hydrogenated amorphous silicon. The shaded areas indicate delocalized states in the bands; these bands themselves have tails of localized states with an exponential distribution. Midway between the bands are levels belonging to gross defects such as dangling Si bonds indicated by the two peaked bands around E_F

state (or molecular "orbital") at a particular energy level E. In a range of energies ΔE, the number of such states per unit volume of the solid is $g(E)\Delta E$.

In Figure 12.9 we have illustrated the density-of-states for hydrogenated amorphous silicon as it has emerged primarily from measurements of electron photoemission [37, 38], optical absorption [39], and electron and hole drift mobilities [40]. In the dark at low temperatures, the states with energies below the Fermi energy E_F are filled by electrons; above the Fermi energy the states are empty. There are two strong bands of states illustrated: an occupied valence band ($E < E_V$), originating with the Si–Si and Si–H bonding orbitals and an unoccupied conduction band ($E > E_C$), originating with "antibonding" orbitals.

12.2.4 Bandtails, Bandedges, and Band Gaps

Between the conduction and valence bands lies an "energy gap" where the density-of-states is very low. Any functional semiconductor, crystalline or noncrystalline, must have such an energy gap. For perfect crystals, the valence and conduction bandedge energies E_V and E_C are well defined, as is the *band gap* $E_G = E_C - E_V$. Interestingly, in disordered semiconductors there are exponential distributions of bandtail states near these bandedges. For the valence bandtail, we write $g(E) = g_V \exp[-(E - E_V)/\Delta E_V]$. The width ΔE_V of this exponential distribution is important in interpreting optical absorption experiments, in which it is usually identified with the exponential "Urbach" tail of the spectrum apparent in Figure 12.2. For a-Si:H, a typical value $\Delta E_V = 50 \times 10^{-3}$ eV. ΔE_V is also used to account for the very slow drift of holes in an electric field (i.e. the hole *drift mobility*) [40, 41]. The conduction bandtail width ΔE_C is much narrower; for

the best a-Si:H materials, it is about 22×10^{-3} eV, but increases markedly for amorphous silicon-germanium alloys [42].

Given the presence of exponential bandtails, the very existence of bandedge energy can reasonably be questioned. Remarkably, detailed analysis of drift-mobility measurements supports the concept of a well-defined bandedge [40, 43]. Most workers consider the bandedge to be the energy that separates electron orbitals that are localized (i.e. have well-defined locations in space) from orbitals that are delocalized. The bandedges are correspondingly termed the conduction and valence band *mobility edges* [44].

Unfortunately, for noncrystalline semiconductors there is no single, conclusively established procedure for locating the bandedges within the density-of-states. The band gap is thus difficult to determine without some ambiguity. Since amorphous silicon–based materials with varying band gaps are used in solar cells, it is nonetheless very important to establish conventional procedures for comparing band gaps. By far the most common approach is to analyze measurements of the optical absorption coefficient $\alpha(h\nu)$ similar to those in Figure 12.2; one typical analysis yields an "optical" or "Tauc" band gap E_T [45]

$$\alpha(h\nu) = (A/h\nu)(h\nu - E_T)^2 \qquad (12.1)$$

The proportionality constant A incorporates several effects and is not usually studied separately.

The band gap obtained using this procedure is typically about 1.75 eV in a-Si:H, but varies substantially with deposition conditions and alloying with germanium or carbon. A simpler procedure than that of Tauc is to define the band gap to be the photon energy corresponding to a particular optical absorption coefficient α; using $\alpha = 3 \times 10^3$/cm yields values (denoted as $E_{3.5}$) similar to the Tauc procedure. Finally, there is undoubtedly a difference between these optical estimates of the band gap and the true, "electrical" band gap $E_G = E_C - E_V$. Internal photoemission measurements [46] indicate that the electrical band gap is 50 to 100 meV larger than the Tauc band gap.

12.2.5 Defects and Gap States

Between the bandtails lie defect levels; in undoped a-Si:H, these levels appear to be due entirely to the dangling bonds ("D-centers") measured by electron spin resonance. For example, infrared absorption at photon energies around 1.2 eV is sensitive to the optical processes that detach an electron from a defect and promote it to the conduction band or that transfer an electron from the valence band to a defect. This infrared signal is visible in Figure 12.2; for samples of varying electronic properties, the infrared absorption coefficient is proportional to the D-center density over a range of at least a factor of 100 in the density [47].

The next issue to be resolved is the positions of the corresponding levels, as illustrated in Figure 12.9. The D-center is "amphoteric:" there are three charge states (with $+e$, 0, and $-e$ charges), leading to two levels (transitions between the $0/+$ and $-/0$ charge states). A *rough* guide to level positions estimated under near-dark conditions is the following. The $(-/0)$ level is about 0.6 eV below E_C in low defect-density, undoped

a-Si:H [48]. The $(+/0)$ level lies about 0.3 eV below the $(-/0)$ levels; the difference between the 2 levels is usually termed the *correlation energy* of the *D*-center [49].

The actual level positions apparently vary between doped and intrinsic a-Si:H [23], between intrinsic samples with varying densities of *D*-centers [48], and possibly between dark and illuminated states [50].

12.2.6 Doping

Doped layers are integral to *pin* solar cells. Doping itself, which is the intentional incorporation of atoms like phosphorus and boron in order to shift the Fermi energy of a material, works very differently in amorphous silicon than in crystals. For example, in crystalline silicon (c-Si), phosphorus (P) atoms substitute for silicon atoms in the crystal lattice. P has five valence electrons, so in the "fourfold coordinated" sites of the Si lattice, four electrons participate in bonding to neighboring silicon atoms. The fifth "free" electron occupies a state just below the bottom of the conduction band, and the dopants raise the Fermi energy to roughly this level.

In a-Si, most phosphorus atoms bond to only three silicon neighbors; they are in "threefold coordinated" sites. This configuration is actually advantageous chemically; phosphorus atoms normally form only three bonds (involving the three valence electrons in "p" atomic orbitals). The final two electrons are paired in "s" atomic orbitals, do not participate in bonding, and remain tightly attached to the P atom. The reason that this more favorable bonding occurs in a-Si, but not in c-Si, is the absence of a rigid lattice. As a thin film of a-Si grows, the network of bonds adjusts to incorporate impurity atoms in a nearly ideal chemical arrangement. In c-Si, it would be necessary to grossly rearrange several Si atoms in the lattice and to leave a number of dangling Si bonds, in order to accommodate the P atom in this configuration. The extra energy for this rearrangement is larger than what would be gained from more ideal bonding of P, and substitutional doping is favored.

Thus, phosphorus doping is a paradox in amorphous silicon. It is, at first, unclear why it occurs at all, since doping involves fourfold coordinated P, and P atoms are generally threefold coordinated in a-Si. This puzzle was first solved in 1982 by Street, who realized that independent formation of both a positively charged, fourfold coordinated P_4^+ and a negatively charged dangling bond D^- can occur occasionally instead of the more ideal threefold coordination [23]. This understanding leads to two important consequences. First, doping is inefficient in a-Si; most dopant atoms do not contribute a "free" electron and do not raise the Fermi energy. Second, for each dopant atom that does contribute an electron, there is a balancing, Si dangling bond to receive it. These defect levels lie well below the conduction band, so the fourfold coordinated phosphorus atoms are less effective in raising the Fermi energy than that in c-Si. Additionally, the negatively charged dangling bonds induced by doping are very effective traps for holes. Since bipolar transport of both electrons and holes is essential to photovoltaic (PV) energy conversion, photons absorbed in doped layers do not contribute to the power generated by solar cells.

12.2.7 Alloying and Optical Properties

The structural and optical properties we have described can be varied substantially by changes in deposition conditions. For example, changing the substrate temperature or the

dilution of silane by hydrogen (in plasma deposition) causes a change in the optical band gap for a-Si:H films over at least the range 1.6 to 1.8 eV [51]; these changes can be ascribed to changes in the hydrogen microstructure of the films. Even larger changes can be effected by alloying with additional elements such as Ge, C, O, and N; alloying is readily accomplished by mixing the silane (SiH_4) source gas with gases such as GeH_4, CH_4, O_2 or NO_2, and NH_3, respectively. The resulting alloys have very wide ranges of band gaps, as we illustrate for a-$Si_{1-x}Ge_x$:H in Figure 12.10. For simplicity, we shall usually refer to these alloys using the abbreviated notation: a-SiGe for a-$Si_{1-x}Ge_x$:H, and so on.

Only some of these materials have proven useful in devices. In particular, a-SiGe alloys with optical gaps down to about 1.45 eV are employed as absorber layer in multi-junction *pin* cells; the narrower band gap of a-SiGe compared to a-Si allows for increased absorption of photons with lower energies [52]. Figure 12.10(a) illustrates how the spectrum of the absorption coefficient $\alpha(h\nu)$ changes for a-SiGe alloys with different atomic percentages x; the different optical band gaps are indicated as labels. Two features of these data should be noted. First, the Urbach slopes remain constant (at about 50 meV) over the entire range of band gaps. Second, the plateau in the absorption coefficient at the lowest photon energies increases steadily as the band gap diminishes, which is indicative of a corresponding increase in defect density.

Figure 12.10(b) is a contour plot showing how the optical band gap of a-$Si_{1-x}Ge_x$:H varies with the Ge-ratio x and with atomic fraction h of hydrogen. The figure reflects experimental results for a-Si:H alloys of varying H-fraction [51] and for a-SiGe:H alloys for which both x and h were reported [53].[5] Note that, for constant fraction h, the band

(a)   (b)
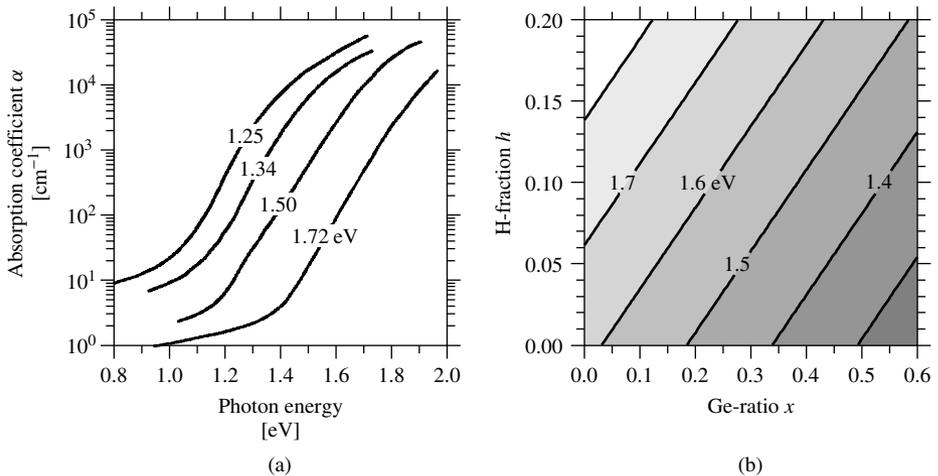
Figure 12.10 (a) Absorption coefficient spectra for a-SiGe alloys; the optical band gaps and corresponding Ge fractions x are 1.25 to 0.58, 1.34 to 0.48, 1.50 to 0.30, 1.72 to 0.0 [52]. (b) Typical optical band gaps for a-$Si_{1-x}Ge_x$:H alloys for varying Ge-ratio x and atomic fraction h of hydrogen

[5] Figure 12.10 is based on the function $E_G = 1.62 + 1.3h - 0.7x$ obtained by fitting to experimental results reported by Hama *et al*. [51] and Middya *et al*. [53].

gap decreases about 0.7 eV as the Ge ratio x increases from 0 to 1. The band gap increases with atomic fraction of hydrogen h. Figure 12.10(b) should be viewed as a useful approximation; in particular, the atomic fraction h is only one aspect of the hydrogen microstructures in a-SiGe alloys, and quantitative deviations from the contour plot are likely. Additionally, only some of the materials represented in the figure are useful as absorber layers. In particular, as the Ge ratio x rises to about 0.5, the optoelectronic properties become so poor that these alloys are no longer useful in solar cells [54]. Similarly, only limited ranges of the atomic fraction of hydrogen h yield useful absorber layers.

It might be thought that a-SiC would be equally useful as a wider band gap absorber; despite some promising research [55], this material is not being used as an absorber layer by manufacturers. B-doped a-SiC is used extensively as a p-type, window layer [56]. a-SiO and a-SiN are used as insulators in thin-film transistors [57], but are not major components in solar cells.

12.3 DEPOSITING AMORPHOUS SILICON

12.3.1 Survey of Deposition Techniques

The first preparations of a-Si:H by Chittick *et al.* [58] and by Spear and LeComber [59] used a silane-based glow discharge induced by radio frequency (RF) voltages; the method is now often termed plasma enhanced chemical vapor deposition (PECVD). Since this pioneering work, many deposition methods have been explored with the intention of improving material quality and deposition rate. Among these methods, PECVD using 13.56-MHz excitation is still the most widely used today in research and manufacturing of a-Si-based materials. However, emerging film deposition methods, mostly toward higher deposition rate or toward making improved microcrystalline silicon films, have been extensively explored in recent years. Table 12.1 summarizes the most extensively studied deposition processes used as well as some of their advantages and disadvantages. Among these, PECVD with very high frequency (VHF) and hot-wire (HW) catalytic deposition

Table 12.1 Various deposition processes used for depositing amorphous silicon–based materials

Processes	Maximum rate^a [Å/s]	Advantages	Disadvantages	Manufacturers	References
RF PECVD	3	High quality uniform	Slow	Many	[60–62]
DC PECVD	3	High quality uniform	Slow	BP Solar	[63, 64]
VHF PECVD	15	Fast	Poor uniformity	None	[65, 66]
Microwave PECVD	50	Very fast	Film quality not as good	Canon	[67]
Hot-wire	50	Very fast	Poor uniformity	None	[68, 69]
Photo-CVD	1	High quality	Slow	None	[70, 71]
Sputtering	3		Poor quality, slow	None	[72, 73]

^{a}Maximum deposition rate: The deposition rate beyond which the film quality deteriorates rapidly; these numbers are empirical, not fundamental limits, and represent current results at the time of publication

process will be further discussed in this section because of their potential for use in future high-throughput solar cell manufacturing.

12.3.2 RF Glow Discharge Deposition

Figure 12.11 shows a schematic of a typical RF PECVD chamber and related parts. A silicon-containing gas such as a mixture of SiH_4 and H_2 flows into a vacuum chamber that is evacuated by a pump. Two electrode plates are installed inside, and an RF power is applied between them; one option is to ground one of these electrodes. At a given RF voltage across the plates, there is usually a range of gas pressures for which a plasma will occur. The plasma excites and decomposes the gas and generates radicals and ions in the chamber. Various substrates may be mounted on one or both of the electrodes, and thin hydrogenated silicon films grow on the substrates as these radicals diffuse into them. The substrates are heated to achieve optimum film quality; this effect is attributed to thermally activated surface diffusion of adatoms on the growing film.

A PECVD system usually consists of several major parts: (1) a gas delivery system (gas cylinders, pressure regulators, mass flow controllers, and various gas valves to direct gas flows); (2) a deposition chamber that has electrodes, substrate mounts, substrate heaters, and the RF power feed through; (3) a pumping system that usually has a turbomolecular pump backed with a mechanical pump; (4) a pressure control system that has a capacitance manometer, ionization gauges, thermocouple gauges, and/or throttle valve to monitor and control the chamber pressure; (5) an exhaust system for the process gases (typically either with a chemical scrubber to neutralize the gases or with a "burn box" to pyrolyze them). In multichamber systems there is a transfer system to move substrates inside the vacuum system between various deposition chambers through appropriate gate valves. Many of these elements are connected to an instrument control panel that contains an RF power supply, impedance matching box, and readouts or controllers for the vacuum gauges, mass flow controllers, throttle valves, pneumatic valves, and turbomolecular pumps.

The film growth in a PECVD process consists of several steps: source gas diffusion, electron impact dissociation, gas-phase chemical reaction, radical diffusion, and deposition [60, 61, 74]. To deposit good-quality a-Si films, the deposition conditions need to be
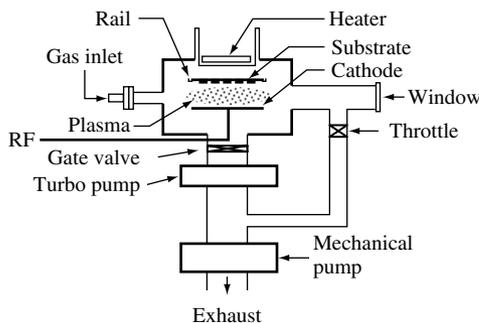

Figure 12.11   Schematic of a typical RF glow discharge deposition chamber

Table 12.2 Ranges of RF-PECVD deposition conditions for a-Si:H films with optimal properties. These numbers are empirical, not fundamental limits, and represent current results at the time of publication

Range	Pressure [Torr]	RF power density [mW/cm^2]	Substrate temperature [C]	Electrode spacing [cm]	Active gas flow^a [sccm/cm^2]	H$_2$ dilution R^b
Upper	2	100	350	5	0.02	100
Medium	0.5	20	250	3	0.01	10
Lower	0.05	10	150	1	0.002	0

^{a}Flows of active gases, such as SiH$_4$, GeH$_4$, or Si$_2$H$_6$, for each unit area of the deposition area (electrode + substrate + chamber walls)
^{b}Hydrogen dilution R, defined here as the ratio of hydrogen and active gas flows (e.g. H$_2$/SiH$_4$)

controlled within certain ranges desirable for high-quality a-Si growth. Typical ranges of parameters for a-Si are summarized in Table 12.2.

The pressure range is usually between 0.05 and 2 Torr. Lower pressure is desirable for making uniform deposition, and higher pressure is more desirable for preparing microcrystalline silicon films. Most researchers use a pressure between 0.5 and 1 Torr for a-Si deposition. The RF power should be set at around 10 to 100 mW/cm^2 for a capacitively coupled reactor. Below 10 mW/cm^2, it is difficult to maintain a plasma. Higher power is desirable for higher deposition rate. However, above 100 mW/cm^2, the rapid reactions in the gas can create a silicon polyhydride powder that contaminates the growing Si film. This problem can be mitigated by using very low pressure or strong hydrogen dilution.

The substrate temperature is usually set between 150 and 350°C. At lower substrate temperature, more H is incorporated in the film. As expected from Figure 12.10, this increases the band gap of a-Si:H slightly [51, 75]. However, lower substrate temperature (<150°C) exacerbates silicon polyhydride powder formation unless high hydrogen dilution is used. At higher substrate temperature, less hydrogen is incorporated and the band gap is somewhat reduced. These effects are attributed to the thermal enhancement of the surface diffusivity of adatoms during growth; presumably at higher temperatures the silicon network is more ideal and binds less hydrogen. Researchers exploit the substrate temperature effect on the band gap in device making. Wider band gap materials are useful in the top component cell of a triple-junction solar cell [76, 77]. Narrower band gap a-Si is useful as the top cell i-layer of an a-Si/a-SiGe tandem cell. However, at temperatures higher than 350°C the quality of the material degrades; this effect is attributed to loss of hydrogen passivation of dangling bonds.

The electrode spacing in an RF glow discharge reactor is usually set between 1 and 5 cm for a-Si deposition. Smaller spacing is more desirable for a uniform deposition, while with a larger spacing it is easier to maintain a plasma. The flow rate that is required is determined by deposition rate and the area of the reactor plates. Some of the silicon atoms in the gases directed into the chamber are deposited onto the substrates or the chamber walls; the remainder gets pumped to the exhaust. Manufacturers may prefer conditions that lead to higher gas utilization (lower gas flows and higher RF power). But this compromises the quality of a-Si films deposited near the downstream area when a linear flow scheme

is used. For an R&D type deposition system with a 200-cm^2 electrode area and for the deposition of a-Si at the rate of 1 Å/s, a few sccm (cubic centimeters per minute at atmospheric pressure) of SiH$_4$ flow is typical. As one may easily calculate, for such a chamber with an electrode diameter of 16 cm and an electrode gap of 2.54 cm, 1 sccm of SiH$_4$ (or 0.005 sccm/cm^2 for this chamber) for a 1-Å/s deposition rate corresponds to a gas utilization of 11%. For the deposition of high-quality, stable a-Si material, a hydrogen dilution at appropriate level is usually used, as will be discussed in Section 12.3.6.

Another important aspect of the growth of high-quality a-Si films is the reduction of contaminants, such as oxygen, carbon, nitrogen, or metal elements. Fortunately, because of the flexibility of the bonding network in an amorphous solid, the tolerance level for contaminants in a-Si is much higher than that of its crystalline counterpart. For example, for one of the cells (with a 1.84-eV intrinsic layer) whose optoelectronic behavior is shown in Figure 12.23, a secondary ion mass spectroscopy (SIMS) measurement [78] reveals that the intrinsic layer has concentrations of O, C, and N around 1.3×10^{19}, 2.2×10^{18}, and 1.7×10^{17}/cm^3. Despite these contamination levels, this cell has a very good efficiency; the contamination levels indicated are typical for a-Si-based i-layers. However, when the amount of contaminants are higher than these in the i-layers, the device performance, particularly the fill factor, will suffer as a result of the reduced diffusion length of photogenerated carriers.

To understand and monitor the film growth in a PECVD process, various spectroscopic tools, including optical emission spectroscopy [79], optical absorption spectroscopy [80], and residual gas analyzer [81] have often been used to measure the plasma and the concentration of various species inside the reactor. It is believed that the SiH$_3$ radical is mostly responsible for the growth of high-quality a-Si film [82]. Such spectroscopic tools could be useful in studying and monitoring the active species and contaminants during growth, especially for process control in manufacturing.

RF glow discharge systems may be designed with different geometries based on specific needs and deposition requirements. While in R&D process the substrates and electrode are usually placed horizontally, in manufacturing processes the substrates are often installed vertically for high throughput production.

12.3.3 Glow Discharge Deposition at Different Frequencies

The standard RF frequency for glow discharge deposition is $f = 13.56$ MHz, which is a frequency allotted for industrial processes by federal and international authorities. A much larger frequency range has been explored, including DC ($f = 0$), low frequency ($f \sim$ kHz), very high frequency (VHF) ($f \sim 20$–150 MHz), and microwave frequency (MW) ($f = 2.45$ GHz). DC glow discharges were used in the early days of amorphous silicon at RCA Laboratories, and they are presently used in manufacturing at BP Solar, Inc. [63, 64]. AC glow discharge, including RF, VHF, and MW PECVD, are more widely used because of the relative ease in maintaining the plasma and because of more efficient ionization. VHF and MW deposition have been intensively studied because of the higher deposition rate both for amorphous and, recently, for microcrystalline and polycrystalline silicon films. In the following, we discuss the use of VHF and MW PECVD for a-Si deposition.

12.3.3.1 VHF glow discharge deposition

The group at Université de Neuchatel [65, 83] has pioneered VHF plasma as a route to higher deposition rates. Figure 12.12 shows a linear increase in the deposition rate of a-Si films as a function of plasma excitation frequency (under constant plasma power). One key to the success of this approach is that higher excitation frequency enables researchers to deposit a-Si films at rates exceeding 10 Å/s, without making polyhydride powder, as is found when deposition rates are increased by increasing RF power at a lower frequency.

The exact reasons for the high-rate, powder-free deposition of a-Si using a VHF plasma are not well understood. At this moment, it is thought that the beneficial effect is due to an enhancement in the high-energy tails of the electron energy distribution function of the plasma [66, 84].

High-quality films and devices have been obtained using VHF deposition [66, 83, 85]. Table 12.3 compares four single-junction solar cells with intrinsic layers fabricated using low and high frequencies and low and high RF power; otherwise the deposition conditions were identical. While for low-power deposition the cell performances are similar, at high deposition rate, the VHF-produced devices are superior
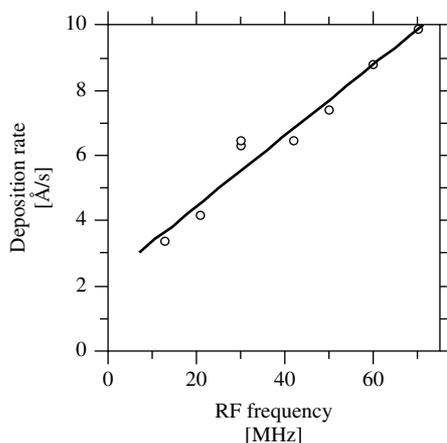

Figure 12.12   Deposition rate for a-Si:H films as a function of RF excitation frequency (at constant power); (After Shah A *et al*., *Mater. Res. Soc. Symp. Proc.* **258**, 15 (1992) [83])

Table 12.3   Comparison of solar cell properties for cells with *i*-layers deposited using RF and VHF frequencies and different deposition rates. The VHF-deposited devices are superior at high deposition rate [85]

Excitation frequency [MHz]	Deposition rate [Å/s]	Initial cell power [mW/cm^2]	Degradation [%]
RF (13.56)	0.6	6.6	14
VHF (70)	10	6.5	10
RF (13.56)	16	5.3	36
VHF (70)	25	6.0	22

in both initial efficiency and stability. The ability to make high-quality a-Si material at high rate using VHF could be very important for high-throughput manufacturing.

Although the advantages of using VHF deposition for high-rate growth have been clearly demonstrated, VHF process had not yet been used in large-scale production at the time of publication of this book. There are two principal challenges to applying VHF deposition in manufacturing. (1) Nonuniform deposition on a large, production-scale substrate. RF standing waves may be formed on the electrode when the electrode size is comparable to half the wavelength of the RF wave. (2) VHF coupling. It is fairly difficult to couple VHF power from the generator to large electrodes. Several research groups are working in this area and have made significant progress [86].

12.3.3.2 *Microwave glow discharge deposition*

Glow discharge deposition at a microwave frequency of 2.45 GHz has also been studied [87, 88]; as expected from Figure 12.12, very high deposition rates are obtained. When the MW plasma is in direct contact with the substrate, the deposited films show poor optoelectronic properties compared with RF-deposited films, and are not suitable as intrinsic layers for high-efficiency solar cells. *Remote* MW excitation has also been studied [89], and high-quality films have been obtained. In remote plasma-deposition processes, substrates are placed outside the plasma region. The MW plasma is used to excite or decompose a carrier gas such as He, Ar, or H_2 that passes through the MW zone toward the substrates. The excited carrier gas then excites SiH_4 or Si_2H_6 directed into the chamber near the substrates. Using such an indirect excitation process, the concentration of SiH_3 radicals can be maintained, while the concentrations of other radicals (SiH_2, SiH, etc.) can be minimized. However, the high deposition rate of the direct plasma deposition is also reduced with remote plasmas. MW plasma deposition has been studied at United Solar [90] and Canon [91, 92], and is used for the deposition of some of the *i*-layers in Canon's 10 MWp triple-junction production line. Generally, the structural and optoelectronic properties of MW-deposited a-Si-based films are poorer than RF-deposited films. However, at a very high deposition rate, for example 50 Å/s, the MW-deposited films will be superior to films made using RF and VHF deposition.

12.3.4 Hot-wire Chemical Vapor Deposition

Several years after Hot-Wire Chemical Vapor Deposition (HWCVD) was introduced [68, 93], Mahan *et al.* [69] improved the deposition process and produced a-Si films with superior material performance. Since then, HWCVD has been studied and used on an experimental scale worldwide for depositing high-quality a-Si- and μc-Si-based films at high rate. The setup for a HWCVD system is similar to the schematic shown in Figure 12.11 for RF-PECVD except that the RF electrode is replaced with a heated filament. In a HW process, SiH_4 gas or a mixture of SiH_4 and other gases such as H_2 or He is directed into the chamber. The gas is catalytically excited or decomposed into radicals or ions by a metal filament heated to a high temperature (around 1800–2000°C). The silicon radicals then diffuse inside the chamber and deposit onto a substrate placed a few centimeters away and heated to an elevated temperature of 150 to 450°C. Mahan *et al.* demonstrated that HWCVD a-Si materials show relatively lower H

content in the film and improved stability against light-induced degradation compared with RF PECVD films [69]. The improved HWCVD a-Si has been incorporated in an n-i-p solar cell as the intrinsic layer and solar cells with ∼10% initial efficiency have been demonstrated [94, 95].

HWCVD is considered very promising. Although it has not yet been incorporated into any of today's large-scale manufacturing facilities, the ability to deposit a-Si and a-SiGe films at very high rate (∼up to 150–300 Å/s) [96, 97] has attracted tremendous interest. Another reason researchers are interested in HW CVD is its effectiveness in making microcrystalline and polycrystalline silicon films.

There are several concerns about incorporating HW processes in manufacturing. First, the uniformity of HW films is still poorer than that of RF PECVD films, although some companies have worked on this and made significant improvement [98]. Second, the filament needs to be improved to reduce the maintenance time in production. Third, HW-deposited solar cells have not yet achieved the same performance as cells prepared using low deposition rate, RF PECVD.

12.3.5 Other Deposition Methods

Beside PECVD and HW deposition methods, other deposition processes have been explored for depositing a-Si films. These include (1) reactive sputter deposition from silicon targets using a mixture of hydrogen and argon [99, 100]; (2) e-beam evaporation, assisted with various hydrogenation methods [101, 102], (3) spontaneous chemical vapor deposition [103], (4) photo-CVD [70, 71] using ultraviolet excitation and mercury sensitization, (5) remote plasma chemical vapor deposition [104], (6) electron cyclotron resonance (ECR) microwave deposition [105, 106], (7) pulsed laser deposition [107, 108], and (8) gas jet deposition [109]. Most of these deposition methods yield poorer a-Si films or solar cells compared with RF PECVD deposited films and devices, and therefore, are not (or not yet) used in large-scale a-Si PV production.

12.3.6 Hydrogen Dilution

Strong hydrogen dilution of the silane gas mixture during a-Si deposition has been found to reduce the density of defect states and improve the stability of the material against light-soaking effects [110–112]. Solar cells with i-layers deposited using strong H_2 dilution show improved performance and stability [113, 114]. There are two other important effects of hydrogen dilution. As the dilution is increased, the deposition rate declines. When hydrogen dilution is increased sufficiently, the thin silicon films that are deposited become microcrystalline.

Ferlauto *et al.* [115] have made a careful study of the "phase diagram" for silicon thin films deposited under varying levels of hydrogen dilution of silane. Some of their results, which are based on *in situ* spectroscopic ellipsometry of the growing film, are presented as Figure 12.13; this diagram pertains to a particular RF power level, substrate (c-Si), and substrate temperature. For lower dilutions ($R < 10$), films are invariably amorphous, but there is a transition to a "roughened" surface beyond a critical thickness. This roughening transition is suppressed as dilution is increased. For higher dilutions, the
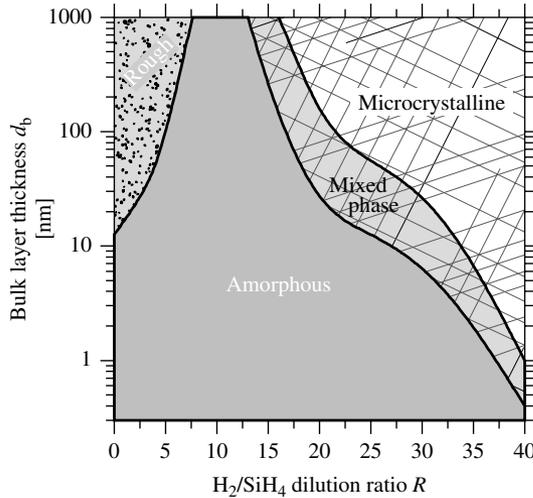
Figure 12.13 Phase diagram for the structure of plasma-deposited silicon thin films for varying dilution ratios R of silane in hydrogen and film thickness d_b; thin films were deposited onto a single-crystal Si substrate. For lower dilutions ($R < 10$) the films remain amorphous, but undergo a roughening transition in thicker films. For high dilutions, films start out as amorphous, develop and silicon crystallites, and ultimately become entirely microcrystalline. Based upon the phase diagram proposed by Ferlauto *et al*. [115] on the basis of *in situ* spectroscopic ellipsometry measurements

growing thin film first adopts an amorphous structure. As the film thickens, crystallites form in the amorphous matrix (creating a "mixed phase"). Ultimately, the film becomes entirely microcrystalline. The details of the phase diagram do depend upon the details of deposition, in particular upon power and substrate conditions, but the structure of the phase diagram is thought to be universal.

These effects of hydrogen dilution during growth are likely owing to the following effects. (1) Atomic hydrogen "etches" a growing film, removing strained weaker bonds that are in energetically unfavorable locations; (2) a high flux of atomic hydrogen promotes the surface diffusivity of adatoms so that they can move around to more energetically stable positions and form stronger bonds; (3) atomic hydrogen diffuses into the network, restructuring it and promoting a more stable structure. For the same reasons, sufficiently large hydrogen dilution induces the formation of microcrystalline Si. The enhancement of short-range and long-range order through hydrogen dilution has been observed in many deposition techniques, including PECVD (DC, RF, VHF, and MW) and HW CVD; of course, the transitions from amorphous to microcrystalline structures occur at different dilution levels for different deposition techniques. There is evidence that the more stable amorphous silicon is deposited under the conditions that are close to the microcrystalline formation [116].

The hydrogen dilution level for the transition from amorphous to microcrystalline silicon thin films depends on other deposition conditions as well. At higher substrate temperatures (above 300°C), the transition from amorphous to microcrystalline state occurs at a higher H dilution; this effect is likely to be due to the low sticking coefficient

of hydrogen on the surface [117]. At the low temperature side (below 250°C), it again takes a higher hydrogen dilution to reach the transition between amorphous to microcrystalline [117]; this effect is likely due to the low surface diffusivity of hydrogen during growth. When a-Si is deposited at a lower temperature with higher H dilution, more H is incorporated and the material has a wider band gap. By following the edge of the transition curve (but staying on the amorphous side) while reducing the deposition temperature, wide-gap a-Si and single-junction a-Si n-i-p cells with 1.053 V open-circuit voltage were deposited [76, 118]. It was also observed that materials deposited near the edge of microcrystalline formation show intermediate-range structural order [119].

12.3.7 Alloys and Doping

As was discussed in Section 12.2.7, a-Si-based alloys can be deposited using a gas mixture of SiH_4 with other gases such as GeH_4, CH_4, O_2 (or NO_2), and NH_3 for obtaining a-$SiGe_x$, a-SiC_x, a-SiO_x and a-SiN_x, respectively. Among these alloy materials, a-SiGe has been explored extensively for PV applications as the narrow band gap absorber. As we see from Figure 12.10, the band gap E_G decreases with increasing Ge content. When E_G is decreased to below 1.4 eV, the defect density becomes so high that the materials can no longer be used as the intrinsic layer for solar cells. Various approaches have been explored to make a-SiGe or a-Ge with low band gap (below 1.3 eV) and low defect density [61]. Despite tremendous progress, device quality a-SiGe with low band gap (below 1.3 eV) has not been demonstrated.

Another related aspect for a-SiGe deposition is the deposition uniformity. Because of the different dissociation rates of germane (GeH_4) and of silane (SiH_4) in an RF plasma, the film deposited near the gas inlet side of the chamber has higher Ge content than the film near the exhaust. This nonuniformity makes it difficult to implement the process over large areas in manufacturing. By taking advantage of the approximately similar dissociation rate of GeH_4 and disilane (Si_2H_6), many research groups use a mixture of GeH_4 and Si_2H_6 for the fabrication of a-SiGe alloy and successfully obtain uniform film [52].

As discussed in Section 12.2.6, a-Si can be doped n-type by mixing phosphine (PH_3) with the gas mixture or doped p-type by mixing diborane (B_2H_6), BF_3, or trimethylboron [TMB, $B(CH_3)_3$] with the gas mixture during deposition. Because of the need for transparency in p-layers, which act as the "window" layer for sunlight, most cells have either μc-Si or a-SiC as the uppermost p-layer. Amorphous SiC p-layers are usually made using a mixture of SiH_4 and CH_4 strongly diluted in hydrogen [61]. The μc-Si p-layer is generally made in a PECVD process using high H dilution with high RF power at relatively low temperature. There have been suggestions that the optimum p-layer for a-Si solar cells is either nanocrystalline or is very close to the transition from amorphous to microcrystalline [120, 121].

12.4 UNDERSTANDING a-Si *pin* CELLS

12.4.1 Electronic Structure of a *pin* Device

Profiles showing electronic levels such as bandedges are an important tool in understanding device physics. Figure 12.14 illustrates the profiles of the bandedge levels E_C and E_V
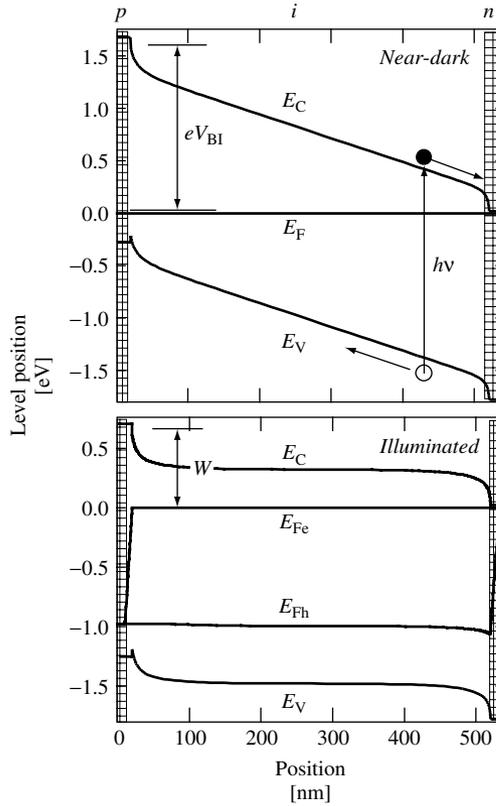
Figure 12.14 Bandedge and Fermi-level profiles in a *pin* solar cell under open-circuit conditions. The open-circuit voltage is precisely the value of E_{Fh} at the left interface ($x = 0$). The built-in potential V_{BI} is illustrated. Note that the *p*-layer has a slightly (0.2 eV) larger band gap than the *i*-layer; the calculation assumes symmetrical offsets of the valence and conduction bands at the *p/i* interface

for an a-Si:H-based *pin* solar cell in the dark and under illumination. The figure is based on calculations using the AMPS-1D$^{©}$ computer program [122, 123] and an idealized set of parameters to describe a-Si:H [124].[6] The electric field $F(x)$ within the device causes all electron level energies such as E_C and E_V to vary in space in the same way; for E_C the expression is $eF(x) = \partial E_C(x)/\partial x$.

Where do these built-in electric fields come from? In isolation, *p*-type and *n*-type materials have very different Fermi energies; in the calculation of Figure 12.14, we assumed that E_F was 1.7 eV below E_C for the *p*-layer and was 0.05 eV below E_C for the *n*-layer. When the *pin* device is assembled, these Fermi energies must be equalized to create thermal equilibrium. Electrons are donated from the *n*-layer to the *p*-layer, which generates a built-in electric field; while the level positions such as E_C and E_V now vary

---

[6] Many computer modeling codes have been developed; Schropp and Zeman give a good overview in Section 6.1 of their monograph [123].

across the device, the Fermi energy itself is constant. The original difference in Fermi energies becomes the "built-in potential" eV_{BI} across the device illustrated in the figure.[7] Electrons and holes that are generated by photon absorption will drift in the built-in electric field in the directions illustrated in Figure 12.14.

The profiles of Figure 12.14 were calculated assuming that the *p*-layer has an electrical band gap of 2.0 eV and that both the middle, intrinsic layer and the *n*-layer have band gaps of 1.8 eV. The use of a wider band gap *p*-layer, which is generally desirable in a-Si:H devices, can both increase V_{BI} and reduce optical absorption in this layer. Because illumination generally enters amorphous silicon cells through the *p*-layer, this layer is also called the cell's *window layer*.

12.4.2 Photocarrier Drift in Absorber Layers

The design of amorphous silicon–based solar cells is strongly affected by how rapidly electron and hole photocarriers drift in an electric field. Ideally, electrons and holes should drift across the cell without interacting with each other, with the electrons ultimately being collected in the *n*-layer and holes in the *p*-layer. If, however, electrons and holes annihilate each other (in other words, if they "recombine" and generate heat), then there will be a loss of power from the cell. In this section, we illustrate one aspect of this loss process, which is the "collapse" of the internal electric field that occurs when the densities of photogenerated, drifting holes and electrons become sufficiently large.

Figure 12.15 is a double logarithmic plot of the mean displacements $L(t)$ for electrons and for holes as a function of the time since their generation by a photon. The results are presented for an electric field $F = 3 \times 10^4$ V/cm, which is about the right magnitude for a 500-nm intrinsic layer under short-circuit conditions. It is important
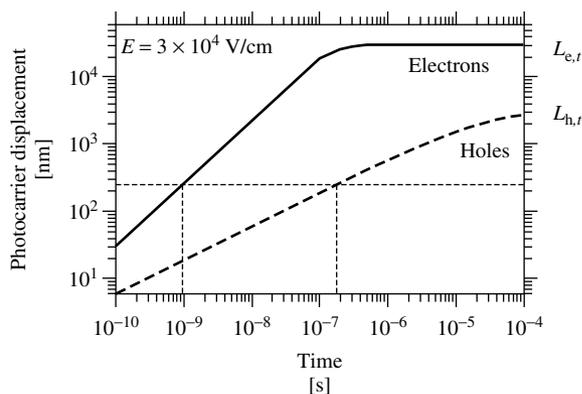

Figure 12.15   Displacements (or drift lengths) of electron and hole photocarriers in a-Si:H as a function of time following generation at room temperature [41]. Note that displacements are proportional to electric field. The saturation in the displacement for longer times (at $L_{e,t}$ and $L_{h,t}$) is due to deep trapping of electrons and holes by defects. Dotted lines illustrate the time required to drift 250 nm

---

[7] We neglect interface dipoles.

to note that these displacements are proportional to electric field. They are based on laser-pulse "time-of-flight" measurements [41].

First consider the electron behavior. For the earlier times (10^{-10} to 10^{-7} s), the displacement is simply proportional to the time, so we can just write the displacement as $L(t) = \mu_e F t$. The parameter μ_e is an electron mobility; it is about 1 cm²/Vs, which is much lower than the mobility for electrons in crystal silicon (about 1000 cm²/Vs near room temperature). For longer times the electron displacement saturates at a value $L_{e,t} = 3 \times 10^{-3}$ cm. This effect is due to the capture of electrons by defects, which is called deep trapping.[8]

Let us briefly consider how these electron parameters affect the functioning of an amorphous silicon cell under short-circuit conditions. The main concern is the possible buildup of electric charge in the cell under solar illumination. If this "space charge density" is too large, then the electric field across the cell will "collapse." A collapsed field reduces the range over which the cell collects carriers, and reduces the cell's efficiency.

We start by determining the travel time of an electron under short-circuit conditions. If the absorber (undoped) layer has a thickness $d = 500$ nm and a built-in potential $V_{BI} = 1.5$ V across it (as for Figure 12.14), then the electric field $E \approx V_{BI}/d$ in the dark is about 3×10^4 V/cm. Note that Figure 12.15 was prepared using this value for E. An electron that is photogenerated near the middle of the absorber layer needs to travel about 250 nm to reach the *n*-layer (moving right across Figure 12.14). Inspection of Figure 12.15 shows that an electron's typical travel time t_T across the absorber layer will be about 1 ns.

We can use this travel time of 1 ns to roughly estimate how much the total charge of electrons builds up under solar illumination. We write $\zeta = j t_T / 2$, where ζ is the total electron space charge in the absorber layer (per unit area of the cell); the factor of 2 implies that the current is carried equally by electrons and holes. For short-circuit conditions with $J_{SC} = 10$ mA/cm², we obtain $\zeta = 5 \times 10^{-12}$ C/cm². To find out whether the built-in electric field is affected by this space charge density, we compare it to the built-in charge density σ_{BI} near the doped layers; σ_{BI} is the charge that actually creates the built-in electric field. Using the standard expression for the charge densities in a parallel plate capacitor, we estimate $\zeta_{BI} = \varepsilon \varepsilon_0 V_{BI}/d$ (ε is the dielectric constant and ε_0 is the "permittivity of the vacuum;" their product is about 10^{-10} C/Vm for silicon). We obtain $\zeta_{BI} \approx 3 \times 10^{-8}$ C/cm². Since ζ_{BI} is about 6000 times larger than the drifting space charge σ of electrons, we conclude that the drifting electrons do not significantly modify the built-in electric field.

We now turn to holes. Two aspects deserve particular attention. First, Figure 12.15 shows that the drift of holes is *much* slower (orders of magnitude slower) than that of electrons. Second, and this also differs significantly from the properties of electrons, the displacement of holes is *not* proportional to time. Instead, the displacement $L(t)$ for holes rises as a peculiar power law with time:

$$L(t) = K(\mu_h/\nu)(\nu t)^\alpha E \tag{12.2}$$

---

[8] Quantitative study of deep trapping involves normalizing of measured values for the drift length $L_{e,t}$ by the electric field E, which yields the "deep-trapping mobility-lifetime product" $\mu\tau_{e,t} = L_{e,t}/E$. $L_{e,t}$ varies inversely with the density of defects in undoped a-Si:H [23, 48].

where the numerical factor K is about unity [125]. This type of *dispersive transport* [126] is actually rather common in noncrystalline semiconductors. The parameter α in the equation is the "dispersion parameter;" μ_h is the "microscopic mobility of holes," and ν is the "escape frequency." Typical parameters for a-Si:H at room temperature are $\alpha = 0.52$, $\mu_h = 0.5$ cm^2/Vs, and $\nu = 8 \times 10^{10}$/s [41]. For a-Si:H, the dispersive transport for holes is explained by the "trapping" of holes in localized, exponential bandtail states just above the valence band (see Figure 12.9). The dispersion parameter α is related to the valence bandtail width ΔE_V by the expression $\alpha = (k_B T / \Delta E_V)$, where $k_B T$ is the thermal energy (k_B is Boltzmann's constant and T is the temperature in kelvins). Electrons in a-Si:H also exhibit dispersive transport, but this is important only below room temperature.

How much does the space charge of holes build up under solar illumination conditions? The simple "travel time" calculation that we used for electrons is not valid for dispersive transport. Instead, we illustrate the effects of hole buildup using a computer simulation. In Figure 12.16, we have presented the electric field profiles $F(x)$ of four widely varying intensities of light; we assume that the light is absorbed uniformly throughout the absorber layer. At low intensities, the electric field is fairly uniform throughout the i-layer. As the illumination flux (and short-circuit current density) rises, the density of holes (and positive charge) builds up. At the highest intensity, the electric field "collapses" at the backside of cell (near the n-layer). In the next section we show how field collapse influences the power generated by a cell. We have chosen to
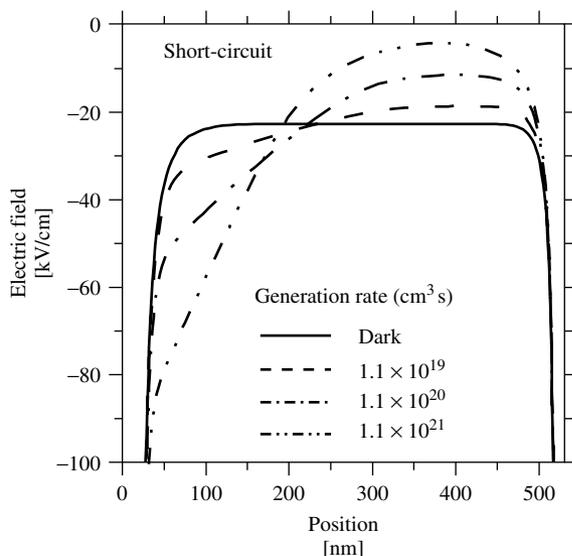

Figure 12.16 Computer calculation (cf. Figure 12.14) of the electric field profile of a *pin* solar cell for several illumination intensities; the cell is under short-circuit conditions. The illumination is uniformly absorbed ($\alpha = 5 \times 10^3$/cm) throughout the i-layer, and the corresponding photogeneration rates are indicated. At low intensities, the electric field is nearly uniform across the intrinsic layer (which starts at a position 20 nm from the origin). As the intensities increase, the electric field collapses nearly to zero close to the n-layer, which starts at 520 nm. The field becomes stronger near the p-layer. At the highest intensity, the fully collected photocurrent density is 11.5 mA/cm^2, which is about the same as that for solar illumination

neglect other aspects of power loss in the cell, which apply when field collapse may be neglected [127, 128], in particular for lower intensities.

12.4.3 Absorber Layer Design of a *pin* Solar Cell

In this section we address the issues that determine the absorber (or "intrinsic") layer thickness. Figure 12.17 illustrates a computer calculation showing how the output power of an a-Si-based *pin* cell varies with intrinsic layer thickness. The differing curves represent results for monochromatic illumination using varying photon energies with the specified absorption coefficients. All the curves were calculated for the same photon flux. Such illumination conditions might be achieved experimentally using a laser whose photon energy could be tuned from 1.8 to 2.3 eV; sunlight, of course, presents a much more complex situation, as we discuss in Section 12.4.6.

　　We first discuss results for illumination through the *p*-layer (solid symbols in the figure). For intrinsic layers that are sufficiently thin, the power is proportional to the number of photons absorbed (i.e. to the product of the thickness d and the absorption coefficient α). In this limit the fill factors have nearly ideal values around 0.8.

　　As the thickness of the cell increases, the power saturates. First consider the behavior for strongly absorbed illumination ($\alpha = 100\,000$/cm – corresponding to a photon energy of about 2.3 eV in Figure 12.2). Power saturation occurs for thickness greater than 100 nm, which is the typical distance at which the photons are absorbed. Since thicker cells do not absorb much additional light, the power stops increasing past this length.
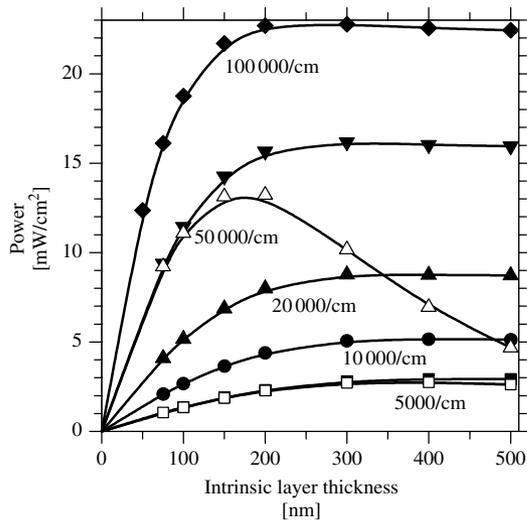

Figure 12.17 Computer calculation of the power output from a *pin* solar cell as a function of intrinsic layer thickness. The differing curves indicate results for monochromatic illumination with absorption coefficients from 5000/cm to 100 000/cm; for typical a-Si:H, this range corresponds to a photon energy range from 1.8 to 2.5 eV (cf. Figure 12.2). Solid symbols indicate illumination through the *p*-layer and open symbols indicate illumination through the *n*-layer. Incident photon flux 2×10^{17}/cm²s; no back reflector

For weakly absorbed illumination (5000/cm – corresponding to a photon energy of 1.8 eV in Figure 12.2), power saturation occurs when the intrinsic layer is about 300-nm thick. This collection length [128] originates in the region where field collapse had occurred in Figure 12.16. The collapsed electric field is strongest near the *p*-layer and weaker near the *n*-layer. It may not be evident, but recombination of electrons and holes occurs predominantly in the weak field regions. This effect can be roughly understood from the following argument. In regions with a field near zero, drift processes driven by electric fields do not determine the densities of photogenerated electrons and holes. Since the electrons and holes are being generated at the same rate, their densities are equal, and they build up under illumination until their rate R of recombination with each other matches the rate G of photogeneration, $G = R$. It is worth noting that these conditions also apply to photoconductivity measurements that are made on isolated films of a particular material.

The asymmetry in the drift of electrons and holes explains why amorphous silicon–based *pin* solar cells are more efficient when illuminated through their *p*-layers. In Figure 12.17 we have also shown (as open symbols) calculations for the power produced by cells that are illuminated through their *n*-layers. Consider first the results with weakly absorbed light (5000/cm). In this case, the photogeneration of carriers is essentially uniform throughout the cells for all the thicknesses shown, and the cells do not "know" which side has been illuminated. Correspondingly, the power generation is essentially the same for illumination through the *p*-layer and through the *n*-layer.

Now consider more strongly absorbed light entering through the *n*-layer (50 000/cm). When the cells are thinner than the absorption length (about 200 nm in this case), the photogeneration is essentially uniform. There is again no difference in the power generated for illumination through the *n*- and *p*-layers. However, for thicker cells, there is a pronounced drop in the power from the cell for illumination through the *n*-layer compared to illumination through the *p*-layer. The power falls because the holes, on average, must drift noticeably further to reach the *p*-layer than when they are generated by illumination through the *p*-layer. The electric charge of the slowly drifting holes builds up and "collapses" the electric field, leading to recombination and loss of power.

12.4.4 The Open-circuit Voltage

In Figure 12.18 we present a summary of the open-circuit voltages (V_{OC}) for a-Si:H-based solar cells from United Solar Systems Corp. as a function of the band gap of the intrinsic absorber layer [129].[9] The measurements were done under standard solar illumination conditions. This graph is quite important for understanding the efficiencies of a-Si:H solar cells. For each photon absorbed, the solar cell delivers an energy $E = (FF)eV_{OC}$. The relation $V_{OC} = (E_G/e) - 0.80$ shows that most cells deliver a voltage that is 0.80 V below the band gap. We can now roughly estimate the power delivered by a cell. For a 500-nm-thick cell and a 1.75-eV band gap, Figure 12.2 shows that a typical photon absorbed by the cell under solar illumination actually carries nearly $h\nu \approx 2.5$ eV of energy. Since fill factors are necessarily less than 1, the energy actually delivered by the cell can be no

---

[9] We have assumed familiarity with the standard solar cell terminology of short-circuit current density J_{SC}, open-circuit voltage V_{OC}, and fill factor FF. See Chapter 3 for definitions of these terms.
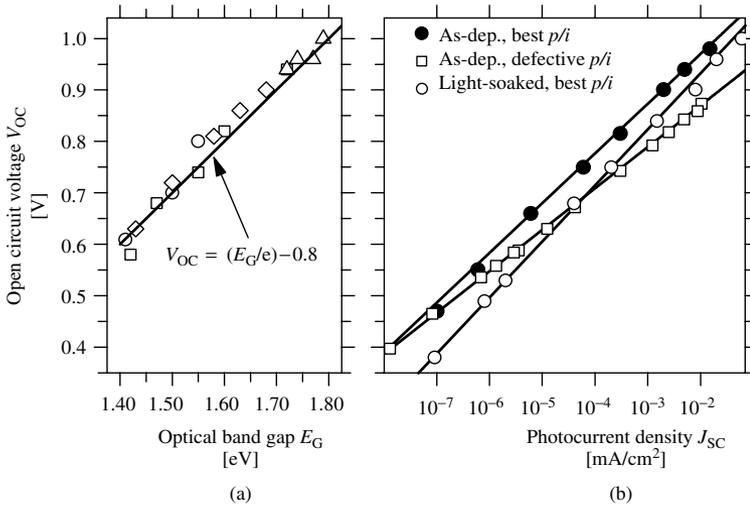
Figure 12.18   (a) Open-circuit voltages for a-Si:H-based solar cells as a function of optical band gap [129]. The band gap variation is mostly due to germanium incorporation. The measurements are from several laboratories; consult the reference for details. (b) Open-circuit voltage V_{OC} versus short-circuit photocurrent density J_{SC} for *nip* solar cells as reported by Pearce *et al.* [130]. The short-circuit current density is proportional to the intensity of the illumination, which had a "white" spectrum similar to solar illumination

larger than 0.95 eV per photon – so over 60% of the absorbed energy must, alas, be lost in such a cell.

The simplicity of the dependence of V_{OC} upon band gap in Figure 12.18 is only possible because open-circuit voltages depend only weakly on (1) the thickness of a-Si:H solar cells and (2) the intensity of illumination. As a result, most details about the cells and measurement conditions are unimportant. For example, in the calculations of Figure 12.17, the open-circuit voltage changed about 10% (from 0.9–1.0 V), while the output power varied from 1 to over 20 mW/cm^2.

Still another simplification applies to many cells. Most workers think that the very best open-circuit voltages in a-Si:H-based cells have reached their "intrinsic limit." This means that these best values are not limited by the details of the *p*- and *n*-type electrode layers [130], but are a fundamental property of the intrinsic layer.

We now give a short argument to explain how V_{OC} is related to the energy profile of Figure 12.14 and why V_{OC} depends only weakly on thickness. The lower panel of Figure 12.14 presents calculated open-circuit profiles of the bandedge levels E_C and E_V of a cell with uniformly absorbed illumination. No Fermi energy is shown in this lower panel because the cell is not in thermal equilibrium – it is exposed to light. Instead, electron and hole quasi-Fermi energies E_{Fe} and E_{Fh} are illustrated, which we will define shortly. Notice that these quasi-Fermi energies merge together at the left edge of the *p*-layer and again at the right edge of the *n*-layer; this merging means that an ordinary Fermi energy can be defined at these edges despite the presence of light. The product eV_{OC} is the difference between these two Fermi levels, as illustrated in the figure. The illuminated

solar cell acts somewhat like an ordinary electrical battery, which also maintains different Fermi levels at its two terminals.

We now define the electron and hole quasi-Fermi energies E_{Fe} and E_{Fh} [131, 132]. For the electron quasi-Fermi energy E_{Fe}, we write

$$n \equiv N_C \exp\left(-(E_C - E_{Fe})/k_B T\right) \tag{12.3}$$

where n is the density of mobile electrons in the conduction band (i.e. in the shaded region of the conduction band in Figure 12.9). N_C is the effective density $(1/cm^3)$ of these conduction band states. A similar expression accounts for the density of holes p in terms of a distinct quasi-Fermi energy for holes E_{Fh} and for the effective density N_V of valence band states.

Interestingly, in Figure 12.14 the hole quasi-Fermi level is nearly constant across the cell, showing sizable variation only where it catches up to E_{Fe} in the n-layer. Similarly, the electron quasi-Fermi level is constant except near the p-layer. This constancy means that the quasi-Fermi levels in the middle of the cell largely determine V_{OC}. The panel also shows that, in the middle of the cell, the bandedge potentials are essentially constant and the electric field is very weak. As mentioned earlier, in such field-free regions the electron and hole photocarrier densities are equal and are determined by the condition that the recombination and photogeneration rates are matched. For cells that have attained the intrinsic limit, it is these fundamental processes that determine V_{OC}.

We now turn to the measured dependence of V_{OC} upon the illumination intensity. Some recent measurements are presented in Figure 12.18(b) [130]. The intensity was varied by using "neutral density" filters that attenuate all photon energies to the same extent. The short-circuit current density J_{SC} has been used as a "surrogate" for intensity based on their proportionality. Consider first the uppermost set of measurements ("as-deposited, best p/i interface"). The logarithmic dependence of V_{OC} upon incident photon flux F is typical of photodiodes [124, 133]. For this sample, the slope of this dependence is determined by the defects; a second line in Figure 12.18 ("light-soaked, best p/i") indicates how the dependence changed following an extended period of light soaking. Interestingly, the difference in the two V_{OC} versus $\ln(J_{SC})$ lines is fairly small (about 0.02 V) under full solar illumination (about 10 mA/cm^2), where the effect of defects upon electron and hole motions is relatively unimportant. This fact partly explains why the dependence of V_{OC} upon band gap can be simple despite the wide variations in defect density for varying materials.

Our previous discussion concerns open-circuit voltages in the intrinsic limit. As might be expected, it is easy to fabricate a-Si:H solar cells with inferior open-circuit voltages. In Figure 12.18, we have also shown the V_{OC} versus $\ln(J_{SC})$ relation [130] for a cell with a (intentionally) defective p/i interface (open squares). This cell was based on the same intrinsic material as the as-deposited cell with the best p/i interface (solid circles); the slope of the V_{OC} versus $\ln(J_{SC})$ relation is now noticeably reduced by the interface effect.

What aspect of nonideal p/i interfaces leads to a reduction in V_{OC}? The physical mechanism through which a poor p/i interface diminishes V_{OC} is the flow of photogener-ated holes from the intrinsic layer (where they are generated) to the p/i interface (where

they recombine with electrons) [124]. The flow means that the hole quasi-Fermi level has a gradient [132] near the p/i interface that reduces V_{OC} below its intrinsic limit. You can just barely notice this gradient effect in Figure 12.14.

The reason this hole current flows is to balance an exactly equal current of electrons. The electrons are being thermionically emitted from the intrinsic layer and over the electrostatic barrier at the p/i interface. You can envision this thermionic process using the bottom panel of Figure 12.14, which shows a barrier of $W = 0.6$ eV for electron emission from the quasi-Fermi level E_{Fe} in the intrinsic material into the p-layer.

The best open-circuit voltages in substrate solar cells are achieved using a boron-doped silicon film [134]. This material is generally referred to as microcrystalline, although extensive characterization of the type presented in Figure 12.13 suggests this p-layer may also be dominated by an amorphous phase. The best open-circuit voltages in super-strate solar cells have been achieved using boron-doped amorphous silicon–carbon alloys (a-SiC:H:B). An indication of the subtlety required to achieve high open-circuit voltages is that cells using a-SiC:H:B p-layers also include a thin (<10 nm) "buffer layer" of undoped a-SiC:H between the p-layer and the intrinsic layer of the cell [135–137]. The precise mechanism by which these buffer layers improve V_{OC} is not conclusively established. We would speculate that the buffer layer impedes electron emission into the p-layer, in accordance with the "thermionic emission" model for the p/i interface effects just described.

12.4.5 Optical Design of a-Si:H Solar Cells

In this section we briefly review the use of *back reflectors* and *substrate texturing,* which are optical design principles that are used to improve the power output of amorphous silicon–based solar cells. The interested reader will find a more comprehensive treatment in the recent monograph of Schropp and Zeman [123] and Chapter 8.

Incorporating a back reflector increases the power output of solar cells. In Figure 12.19, an ideal back reflector doubles the power output for weakly absorbed light (5000/cm in the figure); we are neglecting optical interference and "rereflection" of light by the top of the cell, so the light passes through the cell twice, once on its way down to the reflector, and again on its way back out the top. The back reflector has no effect on power output for strongly absorbed light (50 000/cm in the figure), since that light never "sees" the back reflector. The effects of the back reflector are fairly complex when the thickness, absorption length of the illumination, and collection length for the holes are all comparable, which is what occurs for thicknesses in the range of 100 to 300 nm with 50 000/cm illumination.

For weakly absorbed light, a back reflector for the simple planar structures just described increases power collection about twofold. Much larger improvements may be envisaged. The fundamental idea is "light trapping." An optical beam propagating inside a dielectric structure may be trapped by total internal reflection at the interface with air, which has a lower index of refraction than the dielectric. The principle is the same as that underlying the operation of optical fibers: an optical beam that enters the fiber at one end can travel kilometers without leaving the fiber. For solar cells, the light-trapping idea
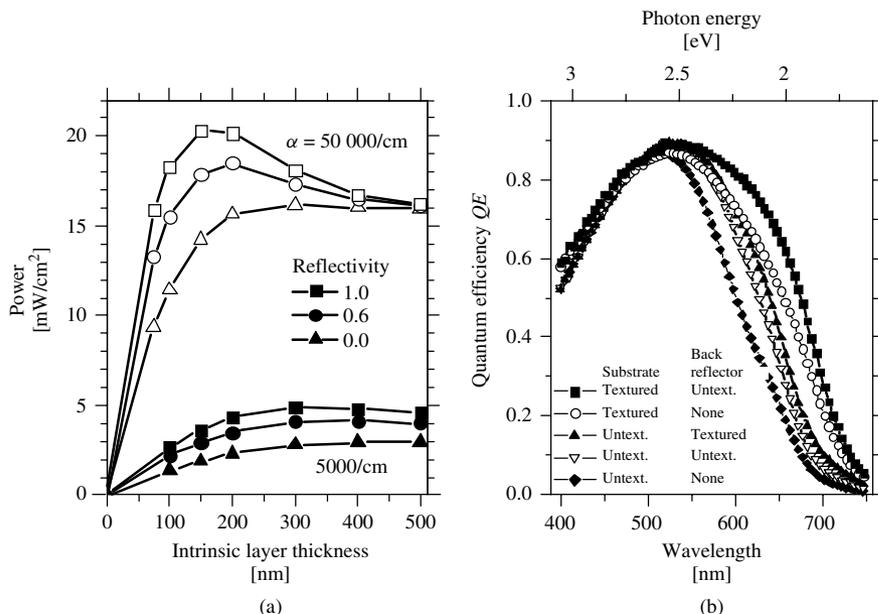
Figure 12.19 (a) Computer calculation of the power output from a *pin* solar cell as a function of intrinsic layer thickness. The two sets of curves indicate results for monochromatic illumination (photon flux $2 \times 10^{17}/cm^2 s$) with absorption coefficients of 5000/cm (black symbols) and 50 000/cm (gray symbols). Results are shown for varying back reflectance; interference effects are neglected. (b) Quantum efficiency (*QE*) spectra for *nip* solar cells deposited under identical conditions, but with two differing substrate textures and differing back reflectors [138]. The sequence of layers in the structure was (TCO/*p*/*i*/*n*/TCO/glass/Ag). The Ag is the back-reflector material (when present); the TCO on top of the glass was either smooth or textured (14% haze).[10] Measured at −1 V bias

implies that a cell might fully absorb light even when its thickness is much less than the absorption length $1/\alpha$ for the light's wavelength.

Light trapping is realized in amorphous silicon (and other) solar cells by using substrates that are "textured" or rough on the same scales as the principal wavelengths in solar illumination. The idea is that the random reflection/diffraction of light by the irregular, textured topography leads to internal reflection. Yablonovitch [139] showed that the maximum gain for such "statistical light trapping" in a textured film on an ideal reflector is $4n^2$, where n is the index of refraction of the film; Yablonovitch's argument is fundamental and not based on any particular form for texturing. For silicon films, with $n \sim 3.5$, the maximum predicted gain is nearly a factor of 50 (for light that is *very* weakly absorbed).

Experimentally, optical gains up to a factor of ten have been reported from the use of textured substrates and weakly absorbed light [138, 140]. In Figure 12.19 we have presented measurements by Hegedus and Deng [138] of the "quantum efficiency" (*QE*)

[10] *Haze* is defined as the percentage of the light incident upon a film that is scattered incoherently. For transparent films, most of the remaining light is transmitted undeviated. Haze depends strongly upon the photon energy. The same value of haze can be obtained from films with quite different morphologies.

for a-Si:H solar cells made with several different textures and back reflectors. The quantum efficiency is defined as the ratio, at a specific photon energy, of the photocurrent density j (A/cm^2) to the incident photon flux f:

$$QE = j/ef \qquad (12.4)$$

Consider first the lowest of the curves (smooth substrate, no back reflector shown with black diamonds). In this sample, photons incident on the p-layer are either absorbed in the cell or pass through the cell and leave it through the glass substrate. The rise of QE as the photon energy increases up to about 2.5 eV is due to the increase in absorption. A -1 V bias was applied, and the resulting electric field prevented the loss of photocarriers to recombination. Near 2.5 eV the QE is nearly one: essentially all incident photons are absorbed and nearly all the photocarriers generated are subsequently collected. The result is sensible. Inspection of Figure 12.2 shows that the absorption coefficient is about 10^5/cm at this energy, so that photons are absorbed within about 100 nm of the top surface of the a-Si:H. Since this length is much smaller than the sample thickness, essentially all photons are absorbed. Some photons are lost because of reflection from the glass and TCO interfaces, which accounts for most of the remaining losses.

For photon energies greater than 2.5 eV, the absorption coefficient continues to increase, so photons are absorbed within a few tens of nanometer at the top of the p-layer. A significant fraction of these photons is absorbed in the p-layer or the TCO; these photons do not contribute to the photocurrent, and so the QE declines for higher photon energies.

Now consider the data for the cell with an untextured substrate (0% haze) and a smooth Ag back reflector (open triangles). For photon energies that are weakly absorbed (below 2.5 eV), the QE increases about twofold because of the back reflector; for strongly absorbed photons, there is little effect of the back reflector. These effects were just explained for the computer modeling of Figure 12.19(a). Interestingly, the use of a textured back reflector further improves the QE. The textured reflector increases the typical angle between the paths of reflected photons and the axis normal to the substrate; this effect increases the typical path length of the reflected photon in the a-Si:H as well as the chance of reflection when a reflected photon arrives back at the top of the cell. The uppermost two curves, with the highest QEs, correspond to cells with textured substrates. For lower photon energies, the textured substrates further improve the QE, although certainly not to the maximum extent $4n^2$ calculated by Yablonovitch. Note also that substrate texturing also leads to a modest improvement of the QE in the blue spectral region (beyond 2.5 eV) due to a reduction in the front-surface reflectance of the cell.

Roughly, the effect of back reflectors and texturing for lower photon energies shown in Figure 12.19 is to reduce the energy threshold for collection of an incident photon by about 0.2 eV. Using Figure 12.2 one can estimate that this reduction in threshold increases the incident solar power absorbed by a 0.5-μm cell from 420 to 520 W/m^2. This estimate is broadly consistent with measurements showing an increase in short-circuit photocurrent under solar illumination of about 25% when textured substrates are used [140–142].

The implementations of texturing and back reflectors, as well as of a front "anti-reflection" coating to reduce the reflection, vary dramatically between superstrate and

substrate cell designs. Superstrate cells usually incorporate a textured, TCO coating on the transparent substrate (usually glass). There are many technologies for producing TCO layers from varying materials (typically SnO_2 or ZnO for a-Si-based cells) and with varying texture and electrical properties. The semiconductor layers are then deposited onto the textured TCO. Plasma deposition of the *p*-layer onto a textured TCO can lead to difficulties: the oxide layer may be chemically "reduced," and achieving ideal properties for a thin *p*-layer could be difficult. Finally, the back reflector deposited on top of the semiconductor layers is often a two-layer structure: a thin TCO layer, followed by the reflective metal (typically Ag – for best reflectivity – or Al – for improved yield in production).

In substrate cells, the semiconductor layers are actually deposited onto the back-reflector, which is again a two-layer structure starting with a textured silver or aluminum metallization and then a textured TCO [143]. Following deposition of the semiconductor layers, a top TCO layer is applied.

12.4.6 Cells under Solar Illumination

In the previous few sections, we have discussed the components of a-Si:H *pin* solar cell design. For monochromatic light and for a given intrinsic layer thickness, we have described the effects of the absorption length and the intensity, the effects of the slow (and dispersive) hole transport and the relatively rapid electron transport, and the use of back reflectors and texturing to enhance the photocurrents realized from weakly absorbed light. In this section we use essentially the same model for these effects as we have in previous sections, but extend it to a cell's operation under polychromatic, solar illumination. In addition, when we changed the band gap, we left all other model parameters unchanged. This discussion continues in the following sections on multijunction (and multi–band gap) cells.

In Figure 12.20 we present calculations of the PV parameters J_{SC}, FF, V_{OC}, and solar conversion efficiency for *pin* solar cells of varying thickness and electrical band gap. First note the increase in short-circuit current J_{SC} as the band gap is reduced (at constant thickness); this effect is due to the increase in optical absorption coefficients in the infrared as the band gap is reduced (cf. Figure 12.10). Also note that the short-circuit current depends only weakly upon thickness beyond the first 100 nm of thickness, which accounts for a substantial fraction of the total absorption. The decline of V_{OC} with band gap of course duplicates the experimental trend of Figure 12.19. Interestingly, V_{OC} remains essentially independent of thickness under solar illumination, despite the "front loading" of the photon absorption. On the other hand, the fill factors under solar illumination are substantially larger than that for uniform illumination. Finally, the differing trends of V_{OC} and of J_{SC} with band gap conspire to determine a maximum efficiency of about 11.3% for a cell with a band gap of 1.45 eV and a thickness greater than about 300 nm. While the neglect of deep levels is too idealized for these calculations to precisely describe the efficiencies, the calculations nonetheless indicate the principal trends of changing the band gap. They also suggest the strategy that has been used to achieve higher efficiencies. In particular, the effects of a decline in V_{OC} with band gap in single-junction cell can be avoided by building multijunction solar cells, as we describe in the next section.
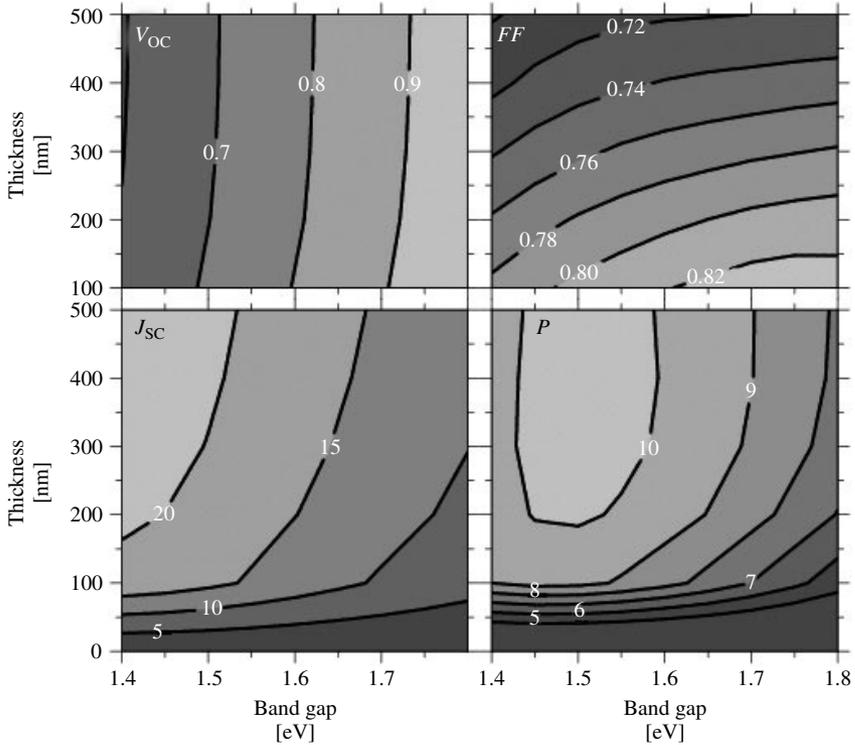
Figure 12.20 Model calculations of the short-circuit current J_{SC} (mA/cm^2), open-circuit Voltage V_{OC}, (V), fill factor FF, and power P under AM1.5 illumination for a-Si:H-based *pin* solar cells with varying intrinsic layer band gaps and thicknesses. No back reflector or texturing effects are included

12.4.7 Light-soaking Effects

In Figure 12.21 we illustrate the power output (standard solar illumination) of a series of cells of varying thickness prepared at United Solar Systems Corp. [14]. The cells are "substrate" type cells prepared on stainless steel. Results are shown both for the initial state of the cells and after 30 000 h (degraded state). For the initial state of the cells, the power rises with thickness and saturates for thicknesses greater than about 400 nm, which is more or less consistent with the modeling presented in Figure 12.17. In their degraded state, the cells reach their maximum power for a thickness of around 200 to 300 nm; substantially thicker cells actually lose some power. As we have noted previously, the degradation effect is correlated with the increase in the defect density in a-Si:H as light-soaking proceeds. Although we did not include defects in the modeling presented in this section, one can understand the degradation effect qualitatively as a result of hole trapping by light-induced defects instead of by valence bandtail states. We do not know whether the fact that the power "peaks" in the degraded state for thicknesses greater than about 300 nm is due to back reflection (cf. Figure 12.19) or due to subtleties in the profile of light-induced defects.
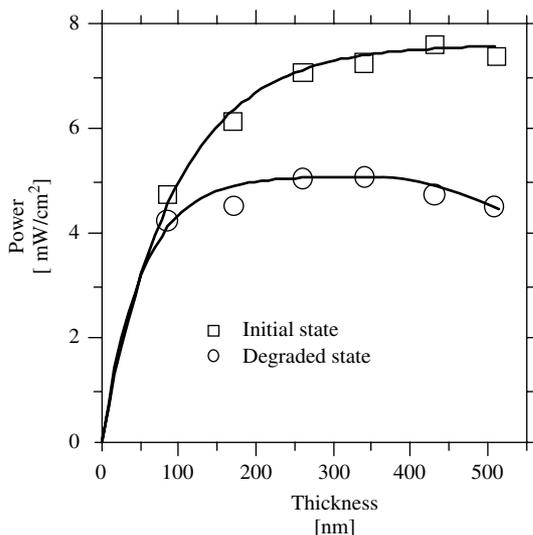
Figure 12.21   Power output (standard solar illumination) for a series of *nip* solar cells with varying intrinsic layer thickness [14]. The degraded state was obtained by 25 000 h of light soaking. The curves are guides only

12.5 MULTIPLE-JUNCTION SOLAR CELLS

12.5.1 Advantages of Multiple-junction Solar Cells

Amorphous silicon solar cells can be fabricated in a stacked structure to form multijunction solar cells. This strategy is particularly successful for amorphous materials, both because there is no need for lattice matching, as is required for crystalline heterojunctions, and also because the band gap is readily adjusted by alloying. Figure 12.4 illustrated the structure of a tandem cell with two junctions (i.e. two *pin* photodiodes) in series. Multijunction, a-Si-based solar cells can be fabricated with higher solar conversion efficiency than single-junction cells and are presently used in most commercial cells.

The fundamental concept underlying multijunction solar cells is "spectrum splitting." Consider what happens if we deposit a second *pin* junction structure on top of a first one. The second structure "filters" the sunlight: photons absorbed in the top junction are of course removed from the light that reaches the bottom cell. We illustrated this filtering effect in Figure 12.2, which shows that 500 nm of a-Si:H absorbs essentially all incident photons with energies greater than 2 eV, and passes photons with smaller energies. In practice, the thickness of the top *pin* junction is adjusted so that it filters out about half of the photons that would otherwise have been absorbed in the bottom *pin* junction.[11] Since the photons that are absorbed in the top junction have relatively large energies, we can use a material with a relatively large band gap as the absorber for this junction, and

---

[11] We discuss only "two-terminal" multijunction cells in this chapter in which a single electrical current flows through the series-connected cells. See Chapter 9 for further discussion of 2, 3 and 4 terminal multijunction cell operation.

we shall obtain a larger open-circuit voltage across the top junction than that across the bottom junction. This is the "spectrum-splitting" effect.

For specificity, consider a tandem cell that bases the bottom junction on material with a 1.55 eV electrical band gap and bases the top junction on material with 1.80 eV electrical band gap material. In the absence of the top, 1.80-eV junction, the 1.55-eV junction might deliver about $J_{SC} = 20$ mA/cm^2 at an open-circuit voltage of 0.65 V. Assuming a fill factor (*FF*) of 0.7, the power output will be 9.1 W/m^2. When assembled in tandem, the current through each junction is about half this value, but the open-circuit voltage will more than double ($V_{OC} = 0.65 + 0.90 = 1.55$ V). The power output rises to 11.2 W/m^2 – for a 19% spectrum-splitting improvement over the single-junction device.

For ideal semiconductors arranged with optimal band gaps, the maximum efficiencies for single, tandem, and triple-junction solar cells under concentrated sunlight are 31%, 50%, and 56%, respectively [144]. Figure 12.22 shows the conversion efficiency contour plot calculated using an a-Si:H-based computer model for two-junction tandem cells; the two axes are the band gaps for the top and bottom component cells [145, 146]. The best efficiency of over 20% occurs with a combination of a 1.8-eV intrinsic layer in the top *pin* junction and a 1.2-eV layer in the bottom. Of course, these model results have not yet been achieved in practice!

We can distinguish three reasons for improved efficiency in a-Si-based multijunction cells over single-junction cells. The first is the spectrum-splitting effect we have just
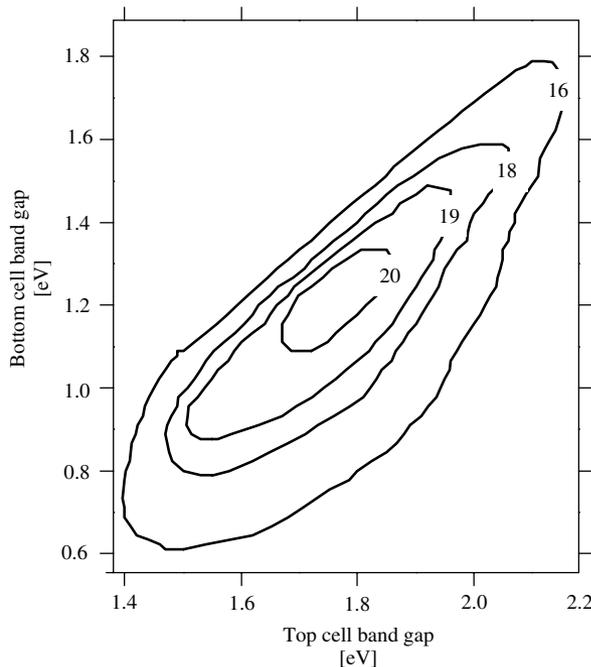

Figure 12.22 Contour plot of constant solar conversion efficiency for a-Si-based tandem solar cells for varying band gaps E_G of the top cell and the bottom cell [145]

described. Second, the i-layers in an optimized, multijunction cell are thinner than in single-junction cells [147, 148]; as can be seen in Figure 12.20, this "junction thinning" means that each individual junction will have a somewhat better fill factor than in the optimized single-junction device, and there will be less change from the initial to the stabilized efficiency of the cell. Third, a multijunction cell delivers its power at a higher operating voltage and lower operating current than a single-junction cell; the lower current reduces resistive losses as the current flows away from the junctions and into its load.

On the other hand, it is more challenging to fabricate multiple-junction solar cells than single-junction cells. The performance of a multijunction cell is more sensitive to the spectrum of the incident light due to the spectrum-splitting feature. This makes it even more critical to control the band gaps and thicknesses of the individual layers. In addition, most multijunction cells incorporate a-SiGe alloys. These alloys are made using germane gas as the germanium source. Germane is several times more expensive than silane and is highly toxic. Manufacturers need to implement strict safety procedures to handle these types of gases. Overall, the advantages and benefits of higher stabilized output power for multiple-junction cells do outweigh the difficulties in the fabrication.

12.5.2 Using Alloys for Cells with Different Band Gaps

As was mentioned in Section 12.2.7, when a-Si is alloyed with other elements such as Ge, C, O, and N, amorphous alloy materials with different band gaps can be obtained. This allows the selection of appropriate band gap combinations for high-efficiency solar cell fabrication. Since the band gap of the a-SiGe alloy can be continuously adjusted between 1.7 and 1.1 eV when different amounts of Ge are incorporated in the alloy, it can be used as the low band gap bottom cell absorber layer for a multijunction solar cell. It is desirable to select a band gap near 1.2 eV to achieve the maximum efficiency according to the contour plot in Figure 12.22. Unfortunately, the optoelectronic quality of a-SiGe degrades rapidly when the a-SiGe band gap is reduced below 1.4 eV, and these materials have not proven useful for PV application.

Figure 12.23 shows the J–V characteristics of a series of a-SiGe solar cells with different Ge concentrations in the i-layer (of constant thickness, and without a backreflector) [149]; the band gaps are indicated in the legend. As the band gap is reduced by incorporating more Ge in an i-layer, V_{OC} goes down and J_{SC} goes up (for a constant thickness), in agreement with trends for the calculations in Figure 12.20. In Figure 12.24, we plot the QE curves of these same a-SiGe cells (along with one curve for a cell with a back reflector, and one curve for a cell with a microcrystalline Si i-layer). Consistent with the increase in J_{SC}, the QE is increased for longer wavelengths (smaller photon energies) as the band gap decreases.

The fill factors of the cells also decrease as the band gap decreases. This effect is due to the increased defect density in the alloyed materials. We have not included this important effect in the discussion previously. As the defect density in the i-layer increases, a given cell's performance will ultimately be dominated by the trapping of photocarriers on defects instead of by bandtail trapping. Roughly speaking, one can think of defect trapping as reducing the "collection length" that determines the useful thickness of the intrinsic layer (cf. Figure 12.17). Naturally, one is principally interested in these effects for the "light-soaked" state achieved by operating cells.
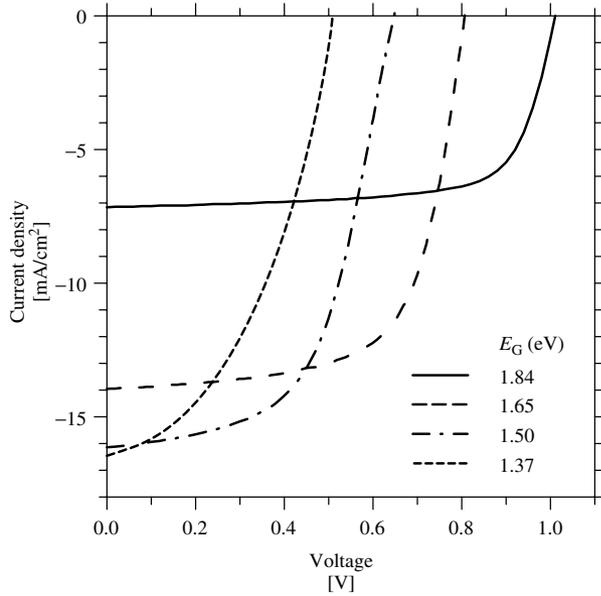
Figure 12.23 Performance of a-Si and a-SiGe *nip* solar cells with different Ge concentrations in the *i*-layer; the *i*-layer band gaps are indicated in the legend. The fill factors for these cells are 0.70, 0.62, 0.55, and 0.43 for the cells with *i*-layer band gaps of 1.84, 1.65, 1.50, and 1.37 eV, respectively [149]
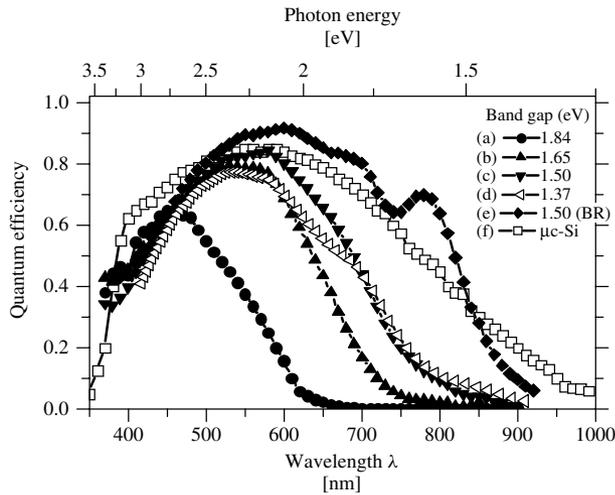
Figure 12.24 Quantum efficiency (*QE*) spectra for a series of a-Si- and a-SiGe-based *pin* single-junction solar cells. Shown in the figure are *QE* curves for single junction solar cells with (a) 1.84 eV a-Si *i*-layer, (b) 1.65 eV a-SiGe *i*-layer, (c) 1.50 eV a-SiGe *i*-layer, (d) 1.37 eV a-SiGe *i*-layer, (e) 1.50 eV a-SiGe *i*-layer, with the device deposited on a back-reflector (BR), (f) μc-Si *i*-layer. Curve (f) is included here for a later discussion in Section 12.5.4. Curves (a) through (e) are from [149] and curve (f) is from [150]

When the Ge content is increased such that the band gap of a-SiGe is reduced below 1.4 eV (see the J–V curve for the 1.37-eV cell in Figure 12.23), the *FF* deteriorates rapidly. In this case, the short-circuit current density does not increase compared to the 1.50-eV cell even though more photons are absorbed. This lack of increase in J_{SC} with further decrease in the band gap occurs because the fraction of photocarriers that recombine has become more significant than the increase in the rate of photocarrier generation.

Similar to the deposition of a-Si, a-SiGe films and devices made with high hydrogen dilution show improved quality and light stability [151]. Optoelectronic properties of narrow band gap a-SiGe material are nonetheless inferior to those of a-Si.

12.5.2.1 Band gap grading

To enhance the fill factor of cells made using a-SiGe, band gap *grading* is used to enhance the collection of holes [152, 153]. In such a design, an asymmetric "V"-shaped band gap profile is created by adjusting the Ge content across the *i*-layer. Wider band gap material lies closest to the *n*- and *p*-layers. The plane of narrowest band gap lies closer to the *p*-layer (through which the photons enter into the device). Such a grading scheme allows more light to be absorbed near the *p*-layer so that "slower" holes do not have to travel far to get collected (see Figure 12.10). Also, the tilting of the valence band assists holes generated in the middle or near the *n*-side of the *i*-layer to move toward the *p*-layer. With appropriate hydrogen dilution during growth and band gap grading, a-SiGe cells can be made to generate up to 24.4 mA/cm^2 (27 mA/cm^2 as the bottom cell in a triple cell) when a light enhancing back reflector is used [154].

12.5.2.2 a-SiC alloys

The band gap of a-SiC can be adjusted between 1.7 and 2.2 eV, depending mainly on the C concentration [155]. After extensive research, most workers decided that a-SiC is not suitable for use as the *i*-layer of the uppermost cell in a multijunction structure. After light soaking, a-SiC material that has an appreciable band gap increase over a-Si is fairly defective and must be used in very thin layers; these layers do not absorb enough sunlight to be optimal. The wide band gap material presently used in triple-junction cells is a-Si with a relatively higher concentration of H (achieved by using lower substrate temperature and H dilution) [8].

12.5.3 a-Si/a-SiGe Tandem and a-Si/a-SiGe/a-SiGe Triple-junction Solar Cells

Several types of multijunction solar cells have been used in a-Si photovoltaics. Dual-junction a-Si/a-Si (same band gap tandem) solar cells have lower material cost than tandem cells using a-SiGe, but have lower efficiencies than more advanced structures [156]. Dual-junction a-Si/a-SiGe cell and triple-junction a-Si/a-SiGe/a-SiGe cells, which use a spectrum-splitting approach to collect the sunlight, achieve higher conversion efficiencies. Some additional details and references may be found later in Table 12.4. Among these, a-Si(1.8 eV)/a-SiGe(1.6 eV)/a-SiGe(1.4 eV) triple-junction solar cells have been used to obtain the most efficient a-Si-based cells today [8]. Figure 12.25 shows the structure of
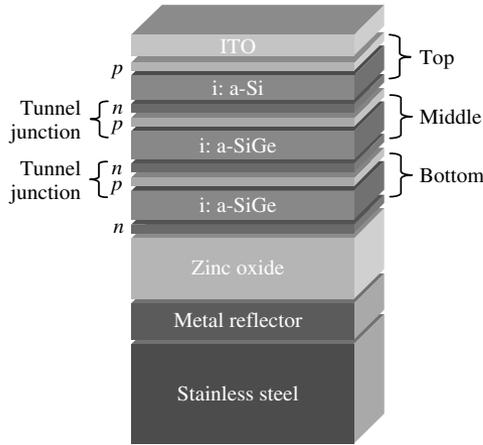
Figure 12.25   Structure of triple-junction *nip* substrate-type solar cells

a triple-junction substrate cell[12] grown on SS foil; a superstrate-type tandem cell (glass substrate) was illustrated previously in Figure 12.4. In both cases, light enters from the *p*-layer so that holes need to travel less distance to get collected than electrons. In the following, we will briefly describe the two designs and typical deposition processes that are most broadly used today.

In *nip* cells deposited on an SS substrate, a reflective metal layer is deposited first on the substrate by sputtering or evaporation, followed by the sputter deposition of a ZnO buffer layer. Usually, silver is used as the reflective layer for research cells because of its high reflectivity, whereas aluminum is used in production because of difficulties with production yield for silver. The metal layer is deposited at high temperature ($300-400°$C); self-segregation in the metal film forms the texture needed for light trapping. The sample is then moved into a RF PECVD deposition system for the deposition of semiconductor layers. The bottom *nip* with an a-SiGe *i*-layer ($1.4-1.5$ eV band gap) is deposited first. A second a-SiGe-based middle cell ($1.6-1.65$ eV *i*-layer band gap) is then added. Finally, the top a-Si-based cell ($1.8-1.85$ eV *i*-layer band gap) is added; the intrinsic layer is made using high H dilution at relatively low temperature. An indium-tin-oxide (ITO) layer is deposited on top via evaporation or sputtering. This layer is approximately 70-nm thick and serves as both the top electrode and an antireflection coating. Metal grids are evaporated or sputter-deposited on top of ITO to further reduce contact resistance.

In *pin* superstrate cells deposited on glass, the glass substrate is first coated with a textured transparent conducting oxide, usually SnO_2 or ZnO, using one of the several methods such as atmospheric pressure chemical vapor deposition (APCVD) [167, 168]. A *pin* top cell having an a-Si *i*-layer is then deposited, followed by the a-SiGe middle cell, and finally the narrow band gap a-SiGe bottom cell. The vertical structure is finished with the deposition of a ZnO buffer layer and metal reflector in the back.

---

[12] Substrate and superstrate cells were illustrated in Figure 12.3. The substrate-type cells are also called *nip*-type cells, and superstrate-type cells are also called *pin*-type cells, corresponding to the sequence in which the layers are deposited.

12.5.3.1 Current matching

In a triple-junction cell, the three component cells are stacked monolithically. Since these component cells are connected in series to form a two-terminal device, the cell with minimum current density during operation will limit the total current of the triple-junction stack. Therefore, the current densities of each of the component cells need to be *matched* (made the same) at the maximum power point for each cell in sunlight. The short-circuit currents J_{SC} of the component cells are only a rough guide to this matching. For an a-Si/a-SiGe/a-SiGe triple-junction cell, the bottom a-SiGe cell usually has the lowest *FF* and the top a-Si cell usually has the highest *FF*. Therefore, the J_{SC} of the bottom cell needs to be slightly greater than the J_{SC} of the middle cell, which in turn needs to be slightly greater than the J_{SC} of the top cell. For an optimized triple-junction cell, the differences in J_{SC} between the bottom and the middle and between the middle and the top cells are each about 0.5–1 mA/cm². This is referred to as an intentional "mismatch" in the J_{SC} values designed to match the cells at the operating point. To obtain the highest stabilized solar cell efficiency, the triple cell needs to be designed, by adjusting the band gaps and thicknesses of the component cell i-layers, such that the component cell currents are matched at the maximum power point in the light-soaked state.

While adjusting for current matching, one needs to consider that the bottom cell benefits from the light enhancement from the back reflector, as can be seen from Figure 12.24, while the middle and top cells receive little benefit from the back reflector.

12.5.3.2 Tunnel junctions

Another area that needs attention in fabricating a multijunction solar cell are the *tunnel junctions* at the interfaces between adjacent *pin* cells. These interfaces lie between n-type and p-type layers, and one might think that they would have electrical properties like classic *pn* junction diodes. However, researchers take advantage of one of the special properties of a-Si material that was discussed in Section 12.2.6: dangling bonds are generated when doping is increased. Carriers that are trapped on defects on one side of the interface can move to traps on the other side simply by quantum mechanical tunneling. This process is sufficiently efficient that it "short-circuits" electrical transport involving the conduction band and valence band states [169]. For this reason, the doped layers at the tunnel junction, particularly the sublayers near the interface, are made with very high doping. The large density of dangling bonds permits the efficient recombination[13] (by tunneling) of holes from the cell below and electrons from the cell above, as illustrated in Figure 12.25. This tunnel junction is reverse-biased under normal operation; it must generate negligible V_{OC} and have negligible resistance and optical absorption [169].

12.5.3.3 I-V measurement

In measuring the $I-V$ performance of a multiple-junction, spectrum-splitting solar cell, researchers need to pay particular attention to the spectrum of the illuminating light

---

[13] One can consider this as a neutralization process.

(see Chapter 16 for more detailed discussion). A triple-junction cell for which the *pin* component cells are current-matched under the standard AM1.5 global spectrum may show poor performance under a different light source, for example, a tungsten lamp. The triple-cell J_{SC} is usually close to the J_{SC} of the limiting component cell except when there is a large mismatch and the limiting cell has a very low fill factor. The V_{OC} of the triple cell is the sum of the V_{OC} of the component cells (and reduced by any photovoltages at the tunnel junctions). It should be noted here that the bottom component cell in a triple-stack generates only about one-third of the photocurrent that it would under full sunlight; therefore, its V_{OC} is slightly smaller (usually by ∼20 mV) than when it is exposed to the full sunlight. The middle cell will have about half the current that it would under the full sunlight. The fill factor of the triple cell depends sensitively on the fill factor of the limiting component cell and on the current mismatch among the component cells. A large mismatch leads to a higher triple-cell *FF*, while on the other hand it also leads to a lower triple-cell current.

12.5.3.4 *Quantum efficiency measurements in multijunction cells*

In measuring the *QE* of a triple-junction solar cell, appropriate light bias and electrical bias need to be applied during the *QE* measurements ([170, 171] or Chapter 16). A direct *QE* measurement without these optical and electrical biases, just as one measures a single-junction cell, would yield a "Λ"-shaped curve, because a current can flow through the cell only if all of the component cells are illuminated simultaneously. When the *QE* of a specific component cell needs to be measured, say the middle cell, a DC bias light is illuminated on the cell through a filter that transmits only blue light and red light so that the top and bottom cells are illuminated. Under this condition, the middle cell current is limiting when the light through the monochromator is absorbed by the cell. Therefore, the current through the sample is that of the middle cell, that is, the AC photo current at the monochromatic light that is absorbed in the middle cell. This AC photocurrent is modulated by an optical chopper, and therefore can be easily detected using a lock-in amplifier.

The other two component cells can be measured in the same way except that different optical filters for the bias light need to be used. When the cells are measured without externally applied electrical voltage bias, the component cell being measured is actually under reverse bias, equal to the sum of the V_{OC} of the other two component cells. In this case, the *QE* curve would indicate the *QE* of the cell under reverse bias condition, which mostly is close to the *QE* under short-circuit condition when the component cell *FF* is high. To measure the *QE* under short-circuit current condition, electrical voltage needs to be externally applied to cancel out the voltage generated by the other component cells under the optical bias light. Figure 12.26 shows the *QE* curves of a triple-junction solar cell measured using this method [158]. The short-circuit current of component cells can be calculated by integrating the *QE* values with the AM1.5 light spectrum. The outer profile in Figure 12.26 is obtained by adding the three component cell *QE* curves. Comparing the *QE* curves in Figure 12.26 and Figure 12.24, the middle cell *QE* is roughly the same as the difference between curves (b) and (a), while the bottom cell *QE* is roughly the same as the difference between curves (e) and (b). The outer profile is roughly the same as curve (e) in Figure 12.24.
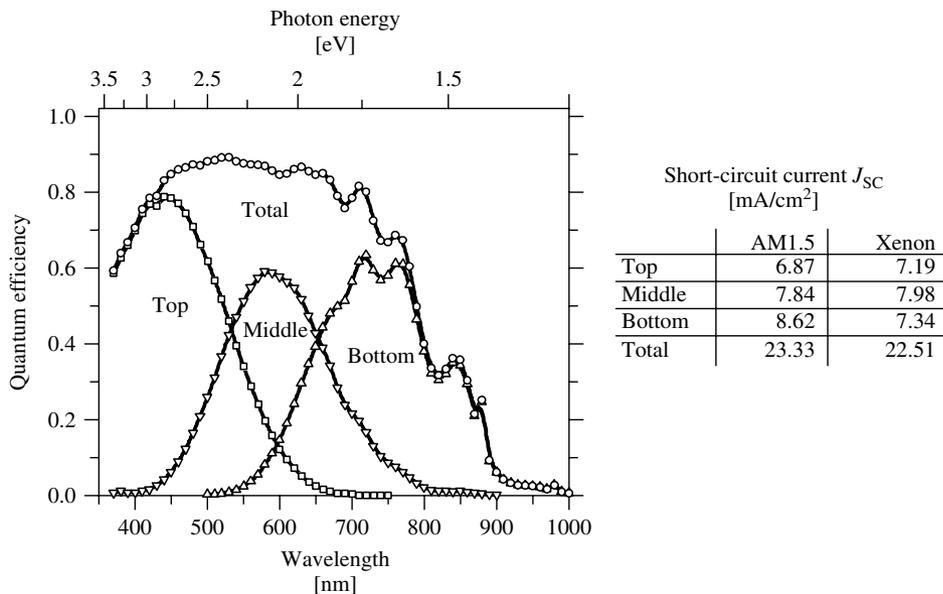
Figure 12.26   Quantum efficiency curves of component cells of a typical triple-junction solar cell. The table indicates the short-circuit current densities J_{SC} for the component cells measured for AM1.5 illumination and with a xenon illuminator [158]

12.5.3.5 *Matching component cells in multijunction designs*

In matching component cell currents in the triple cell design, researchers usually take the following steps. Take the triple cell in Figure 12.26 as an example. The design is largely dictated by the bottom a-SiGe component cell. If this component cell were fabricated on the back reflector as a stand-alone single-junction cell, it would have a short-circuit current around 23 mA/cm² and a *QE* curve similar to the one labeled "Total" in Figure 12.26. In order to achieve current matching in the triple cell, a stand-alone, single-junction version of the middle a-SiGe component cell (without a back reflector) needs to generate about two-third of the bottom cell's current. The band gap and/or the thickness of the a-SiGe middle component cell's *i*-layer are then adjusted to accomplish this. Finally, the top component cell's thickness is adjusted to obtain one-third of the bottom cell's current (again, without a back reflector). In this way, all three cells would have the same current when they are stacked in series.

In Figure 12.26, the long-wavelength behavior of the *QE* curves for each of the component cells is determined by the component cell's *i*-layer thickness and band gap, and (for the bottom component cell) by the back reflector performance. However, the short-wavelength behaviors for the middle and bottom component cell's *QE* curves are largely determined by the thicknesses and band gaps of the top and middle cells, respectively, since these component cells act as filters for the shorter wavelength (higher energy) photons. The short-wavelength behavior of *QE* for the top cell is sensitive to the absorption of ITO and top cell *p*-layer as well as the loss of electrons that are diffused back to the *p*-layer and get trapped.

Table 12.4 Efficiency of small-area solar cells fabricated in different laboratories

Structure	Initial η [%]	Stable η [%]	Organization	References
a-Si/a-SiGe/a-SiGe	15.2	13.0	United Solar	[8]
a-Si/a-SiGe/a-SiGe	11.7	11.0	Fuji	[157]
a-Si/a-SiGe/a-SiGe	12.5	10.7	U. Toledo	[158]
a-Si/a-SiGe/a-SiGe		10.2	Sharp	[159]
a-Si/a-SiGe	11.6	10.6	BP Solar	[160]
a-Si/a-SiGe		10.6	Sanyo	[161]
a-Si/μc-Si		12.0	U. Neuchatel	[162]
a-Si/μc-Si	13.0	11.5	Canon	[163]
a-Si/poly-Si/poly-Si	12.3	11.5	Kaneka	[164]
a-Si/a-SiGe/μc-Si	11.4	10.7	ECD	[165]
a-Si/a-SiGe		12.4	United Solar	[166]

12.5.3.6 High-efficiency multiple-junction solar cells

Table 12.4 above lists some properties of multiple-junction solar cells fabricated in selected laboratories around the world. The degradation of multiple-junction solar cells is usually in the range of 10 to 20%, while the degradation of single-junction solar cells is usually in the range of 20 to 40%. These percentages apply to the cell's properties after 1000 h of light soaking under 1 sun light intensity at 50°C, which is the standard protocol used for gauging light degradation today. The degradation of triple cells is smaller because (1) the i-layers are thinner and (2) each i-layer absorbs only one-third of the total current, therefore having less photogenerated recombination in the i-layer. As one can see from the table, the highest stabilized cell efficiency is 13.0% for a triple-junction device structure made at United Solar Systems Corp. Table 12.4 also includes the best solar cells made using μc-Si as a component cell. The highest stable efficiency so far using a-Si/μc-Si tandem structure is 12% for a cell made at Univ. of Neuchatel using VHF plasma deposition.

12.5.4 Microcrystalline Silicon Solar Cells

Microcrystalline silicon (μc-Si) has been studied extensively for three decades [172] and has been used for doped layers in a-Si solar cells for over 15 years [134, 173]. Because of the difficulties in passivating the defects located at the grain boundaries, μc-Si was not actively considered as an intrinsic layer in the *pin* or *nip* type solar cells until 1992, when Faraji *et al.* [174] and Meier *et al.* [150] reported the fabrication of μc-Si–based *pin* solar cells using VHF PECVD. Since then, μc-Si and poly-Si solar cells have been fabricated by a number of research groups [163, 175–177].

A *QE* curve for such a μc-Si-based cell was presented in Figure 12.24. One can see that the μc-Si has a larger *QE* than the a-Si and a-SiGe cells at longer wavelengths (>850 nm). The total photocurrent generated from a μc-Si cell has reached 26 mA/cm^2 [150, 176]. Therefore, such cells are suitable for use as the bottom cell of a multijunction cell with a-Si-based cells as the top cell. The advantages of using μc-Si as the narrow band gap cell instead of a-SiGe are (1) the higher *QE* in the long-wavelength

region, (2) negligible light induced degradation, (3) reduced materials cost, since μc-Si can be made using SiH_4, which is a relatively low-cost gas compared to GeH_4, and (4) μc-Si cells can be made with high *FF*. On the other hand, the concerns associated with using μc-Si compared to a-SiGe bottom cell are (1) μc-Si cells require much thicker *i*-layers (several micrometers thick) to absorb the sunlight; this is an effect of the lower interband absorption coefficients in (indirect band gap) crystals compared to amorphous semiconductors, (2) the deposition rate for μc-Si material is generally low, so that a much longer time is needed to complete the deposition of a thick μc-Si layer than what is needed for an a-SiGe layer, and (3) μc-Si solar cells have lower V_{OC} (around 0.53 V) than do a-SiGe cells yielding the same J_{SC}.

Beside VHF technique, μc-Si has also been deposited using other high deposition rate methods such as HW CVD [178], GasJet/MW deposition [179], and high-power/high-pressure RF deposition [180]. A typical deposition rate for an a-SiGe *i*-layer is 3 Å/s; to complete a μc-Si cell with comparable deposition time, one would need to deposit μc-Si with at least ~20 to 30 Å/s deposition rate so that it would not be rate-limiting during production.

12.5.5 Micromorph and Other μc-Si-based Multijunction Cells

Meier *et al*. [181] used an a-Si *pin* junction as the top component cell and a μc-Si *pin* as the bottom component cell for a-Si/μc-Si tandem cells; they named these cells *Micromorph* devices. The 1.7 eV/1.1 eV band gaps for the top/bottom cell provide a nearly ideal band gap pair for tandem cells (see contour diagram in Figure 12.22 above).

In order for an a-Si/μc-Si tandem cell to have comparable performance as an a-Si/a-SiGe cell, the bottom cell μc-Si must have at least 26 mA/cm^2 current density. Since μc-Si has an indirect band gap, generating such a high current requires the μc-Si layer to be several micrometers thick. In addition, advanced light enhancement schemes need to be used. In order to maintain current matching in a micromorph cell, the top a-Si component cell must generate 13 mA/cm^2 (i.e. half the current for a stand-alone μc-Si). In addition, this a-Si cell needs to be stable under light so that the tandem cell could be stable.

Two approaches were taken to accomplish this [182, 183]. First, the a-Si *i*-layer is made at a relatively higher temperature, so that there is a lower H concentration (and a reduced band gap, ~1.65 eV). Secondly, a semireflective layer was inserted at the tunnel junction between the top and the bottom cell. This semireflective layer permitted current matching (enhancing the top component cell current at the expense of the bottom cell). With these two approaches, 13 mA/cm^2 J_{SC} was obtained from the top cell with a 3000 Å thick a-Si layer. Innovative approaches need to be taken to further increase the current beyond the present level. With the micromorph tandem design, solar cells with 11 to 12% stable efficiency have been fabricated [163, 183].

One can also combine a-Si and μc-Si cells to fabricate a-Si/μc-Si/μc-Si triple cells. Such a design would relax the stringent requirement on the a-Si top cell due to current matching since it now only needs to generate one-third of the bottom cell current. However, the presently low V_{OC} of a μc-Si cell militates against the triple-junction design.

Still another approach to a triple-junction cell design is to combine a 1.8 eV a-Si top cell, a 1.6 eV a-SiGe middle cell, and a 1.1 eV μc-Si bottom cell [165]. Such a cell design would have the advantages of a thinner and more stable top cell than for a micromorph tandem cell, would have better long-wavelength collection, and would reduce consumption of (expensive) GeH_4 gas compared with an all-amorphous, a-Si/a-SiGe/a-SiGe triple-junction cell.

12.6 MODULE MANUFACTURING

Although the stabilized conversion efficiency of a-Si-based solar cells is presently lower than those of several other types of solar cells, a-Si-based PV products are highly attractive for terrestrial applications since they can be produced using low-cost manufacturing methods. The a-Si PV products are environmentally friendly. They are made mostly using silicon, which is abundant on earth. In addition, the a-Si PV products can be made lightweight, flexible, and radiation-resistant. These make them highly desirable for portable power applications as well as for space power applications. Furthermore, the fact that a-Si products have higher stabilized power output at higher temperature makes these products more desirable in warm weather environment.

During the past 10 years, there has been a rapid increase in the worldwide a-Si production. Presently in 2002, the total worldwide a-Si production capacity exceeds 85 MW/year, including about 30 MW at United Solar Systems Corp. (USA), 20 MW at Kaneka Corp. (Japan), 10 MW at BP Solar, Inc. (USA), 10 MW at Canon (Japan), 6 MW at Sanyo (Japan), 3 MW at EPV (USA), 2 MW at Sovlux (Russia), and several 1-MW plants in various companies in different parts of the world.

These production facilities can be roughly divided into two major categories: those with substrate-type a-Si PV products and those with superstrate-type a-Si PV products. To transform small-area R&D developments into any type of large-scale manufacturing, key issues including uniform deposition over large areas, process gas utilization, deposition rate, production throughput, process reproducibility, machine maintainability and serviceability, process automation, and production yield must be addressed.

For a large-scale production line, in-line processes have been used by all major manufacturers. In the following, we use the production process at United Solar as the example for the substrate-type process and that at BP Solar as the example for the superstrate-type process.

12.6.1 Continuous Roll-to-roll Manufacturing on Stainless Steel Substrates

The continuous, "roll-to-roll" a-Si PV manufacturing process was developed by Energy Conversion Devices, Inc. (ECD) and has been used by ECD's PV joint ventures and partners (United Solar, Sovlux, and Canon) [184–186]. Roll-to-roll refers to the process whereby a "roll" of flexible SS is unrolled and fed into the manufacturing process, and then the SS is again "rolled up" after a manufacturing step has been completed. The production process can be separated into two distinct parts: the front-end coating process and the back-end module assembly process.

The front-end process consists of four continuous, roll-to-roll steps in separate machines: (1) substrate washing, (2) sputter deposition of the back reflector, (3) a-Si semiconductor deposition, and (4) ITO top electrode deposition. Rolls of magnetic SS web, typically 125 µm thick, 0.35 m wide, and 700 m long, are guided through these roll-to-roll machines by magnetic rollers. The roll is unwound from a modular "payoff" chamber on one side and wound up in a modular "take-up" chamber on the other side. Figure 12.27 is a photo of front-end facilities at an ECD designed 2-MW plant, operated by Sovlux, and showing all four roll-to-roll machines.

In the roll-to-roll washing machine, the SS web is guided through ultrasonic detergent cleaning stations with spinning brushes rubbing the surface, multiple deionized water rinse baths, and an infrared drying chamber. An oil-free, particle-free, clean SS roll is then wound up with protective interleaf.

The roll is then unloaded from the take-up chamber of the wash machine and loaded into the payoff chamber of the back-reflector sputter machine. In this machine, the SS web is pulled through several DC magnetron sputter deposition zones with metal targets (Al, Ag, or other alloys) for the reflective layer and ZnO targets for the deposition of ZnO buffer layer. The substrate is maintained at elevated temperature during sputtering so that the metal films develop a texture useful for optical enhancement [185, 187].

The roll is then loaded into the RF PECVD machine for the continuous roll-to-roll deposition of nine layers of semiconductors (*nip/nip/nip*) as well as all of the buffer layers on both sides of a-SiGe absorber layers. The deposition of the different layers occurs sequentially but in a single pass. Innovative "gas-gate" design allows the manufacturer to isolate the feedstock gases in different chambers and to prevent cross-contamination, while at the same time the web passes through the sequence of chambers continuously. The gas gate utilizes laminar gas flow to effectively isolate the gases in adjacent chambers.

Figure 12.27   A photograph of the Energy Conversion Devices, Inc. 2-MW plant showing all four front-end roll-to-roll machines for washing, back reflector sputter deposition, PECVD deposition (right-hand side) and TCO deposition [185]

After the semiconductor deposition, the roll is then loaded into the TCO deposition machine, which uses either reactive evaporation of indium in oxygen ambient or sputtering from an ITO target in an argon atmosphere. The thickness of the ITO is carefully monitored to achieve antireflection properties.

The four roll-to-roll steps are currently not integrated into one machine. This design reflects the different pressure ranges for the four machines: atmospheric pressure for the washing, a few mTorr for back-reflector sputtering, around 1 Torr for PECVD, and a few mTorr for TCO sputtering.

At this point, the SS roll is a giant solar cell, 700 m long, which needs to be converted into many smaller series connected cells to get higher voltage for the modules. The semiautomatic back-end process for cell interconnect and module assembly includes the following steps. The roll of TCO coated a-Si solar cells is first cut into slabs of selected sizes with a slab cutter. Etching paste is then applied to the edge of the slab and activated through a belt furnace to remove ITO around the perimeter of the slab and to define effective solar cell area. Selected small samples (coupons) are collected throughout the run for quality-assurance and quality-control (QA/QC) evaluation. The standard slabs then go through a shunt passivation process in an electrolyte bath to remove and isolate small shunts by converting the TCO at the shunting point into an insulator [188]. The grids, either carbon paste or copper wire coated with carbon paste, are then applied to the slab to complete a strip cell, which is a big cell that generates $\sim$2.3 V voltage and $\sim$2 A current. Different numbers of strip cells, depending on the module specification, are connected together in series with the grids/bus bar of one strip cell connected to SS substrate (the opposite electrode) of the neighboring strip cell. By-pass diodes are also installed at this step for the strip cell protection. The connected cells are then covered with ethylene vinyl acetate (EVA) and Tefzel, which are transparent encapsulating layers, and cured in an oven for appropriate time for lamination. This is then followed by selected module framing.

Despite the need for relatively labor-intensive module assembly process at the moment, the continuous roll-to-roll production of a-Si solar panels on SS substrate has a number of advantages. The product is lightweight and flexible. The front-end production process requires low maintenance and can be easily scaled up. The coated SS roll may be cut into slabs of various sizes to make different products. For example, small sizes are suitable as battery charger, and large sizes as metal roof shingles (more than 5 m long). A high production yield can be maintained. The disadvantage is the need for labor-intensive cutting, gridding, and interconnecting individual cells to create a module.

In the process at Iowa Thin Films, Inc., a flexible Kapton[14] substrate is used. The cell interconnect is achieved by laser scribing, similar to the process at BP Solar for superstrate-type solar cells, as to be described below.

12.6.2 a-Si Module Production on Glass Superstrate

The manufacturing of a-Si solar panels on glass superstrates is being developed by several companies including BP Solar, Inc. (USA), Energy Photovoltaics, Inc. (USA), and

---

[14] ®Registered trademark of the Dupont Corporation.

Phototronics Solartechnik GmbH (Germany) [189]. A typical process is that of BP Solar's 10-MW plant (TF1) in Toano, Virginia, (USA) [190].

The process begins with large sheets of "float" glass, 3 mm thick, with a typical size of 1 m by 0.5 m. A textured tin oxide TCO layer is deposited using an APCVD process either at the glass supplier's plant or at the PV plant. The substrate is edge-polished and cleaned before silver frits are applied as bus bars and cured in a belt furnace. This TCO layer is "scribed" by a laser into strips about 9 mm wide. The substrates are then loaded in the PECVD machine for the deposition of the six semiconductor layers for an a-Si/a-SiGe *pin/pin* tandem structure. The semiconductor deposition is followed by the deposition of a ZnO buffer layer. Another laser scribing is done at this point adjacent to the first scribe lines. This second scribing is done at a lower laser power so that, while the ZnO and a-Si layers are scribed, the underlying tin oxide layer remains intact. An aluminum layer is sputter-deposited as the back reflector and back contact. A third scribing of the Al adjacent to the second completes the interconnection of neighboring cells in series, as shown in Figure 12.28. A fourth, high-power laser scribing around the perimeter of the solar panel isolates the active area from the edges. The panel is then finished by bonding a second glass plate onto the cells with EVA. This second piece of glass is needed for encapsulation, which unfortunately adds weight and cost to the module.

12.6.3 Manufacturing Cost, Safety, and Other Issues

An important aspect of any manufacturing process is cost, which generally consists mostly of raw materials, labor, capital depreciation of the machines, and administration. The overall production cost per unit of product is reduced as the production volume goes up. At a high production volume, perhaps 100 peak megawatts/year, 100 MW_p/year, (under illumination yielding peak power production), the cost is expected to be lower than $1/Wp. Currently, for a-Si modules intended for outdoor use for extended time, the major costs are the module framing, encapsulation, and the substrates (glass or SS). As an example, for the materials cost, the current breakdown at BP Solar's 10-MW plant is 33% for framing and packaging, 38% for TCO/glass, 17% for germane, 7% for encapsulation, and 5% for silane and other feedstocks [63].

Another important aspect with regard to a-Si PV manufacturing is the plant safety. Although there is no toxic material in the final product, the manufacturing processes do involve toxic and pyrophoric gasses such as germane, phosphine, trimethylboron, silane, hydrogen, and so on. Amorphous Si PV manufacturers, who have learned and borrowed
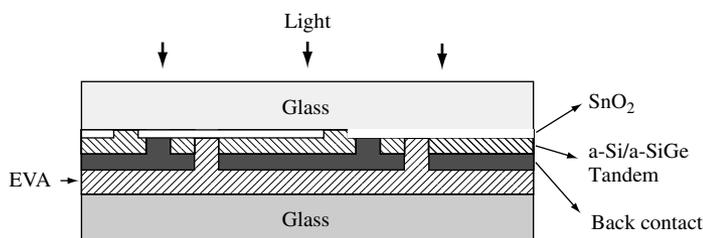

Figure 12.28   Cell interconnection of superstrate-type solar cells, used at BP Solar

heavily from the safety procedures developed by the integrated circuit industry, use a variety of methods to improve the safety of workers. Toxic gases are diluted in hydrogen or silane to 1 to 20%. Gas cylinders are installed outside the building or in fireproof gas cabinets. Toxic gas monitors are installed throughout the plants. Automatic gas isolation and operation shutdowns are implemented. These, among other safety procedures, ensure safe operations in these plants.

The solar conversion efficiency of production modules is generally lower than the efficiency of the research and development (R&D) scale, small-area solar cells since production processes are more restrained by cost reductions. The differences in efficiency are mostly from the TCO performance, semiconductor material quality, deposition uniformity, encapsulation loss, bus bar shadow loss and electrical loss, and small shunts. Rech *et al*. provided a detailed analysis in the efficiency differences between R&D and manufacturing at Phototronics, Germany [191].

12.6.4 Module Performance

Two aspects of PV modules are generally evaluated: maximum solar conversion efficiency and environmental stability. Table 12.5 lists PV modules produced by selected organizations around the world; the table separately lists modules made in R&D type machines (area about 0.1 m^2) and large-area modules (area 0.4 m^2 or greater), mostly produced from production lines. Presently in 2002, large-area modules, with approximately 8% stable efficiency, are manufactured at United Solar and BP Solar and are commercially available in large quantities.

Photovoltaic modules are also evaluated through various environmental tests, as listed in UL, IEC, and IEEE standard testing procedures (see Chapter 16 for more on module testing). These tests generally include thermal cycles between −40 to 90°C; humidity freeze cycles between −40 to 85°C at 85% humidity; hail impact; wet hi-pot

Table 12.5 Stabilized efficiency of a-Si PV modules manufactured by various companies

Structure	Stable η [%]	Size [m^2]	Company	Reference
R&D modules				
a-Si/a-SiGe/a-SiGe	10.5	0.09	United Solar	[186]
a-Si/a-SiGe	9.1	0.08	BP Solar	[160]
a-Si/a-SiGe	9.5	0.12	Sanyo	[192]
Large-area modules				
a-Si/a-SiGe	9.3	0.52	Sanyo	[193]
a-Si/a-SiGe/a-SiGe	9.0	0.32	Fuji	[160]
a-Si/a-SiGe	8.1	0.36	BP Solar	
a-Si/a-SiGe/a-SiGe	7.9	0.45	United Solar	
a-Si/a-Si/a-SiGe	7.8	0.39	ECD	[185]
a-Si/poly-Si	10.0	0.37	Kaneka	[194]

test and light soaking. PV modules that are sold for commercial use have generally been qualified by these testing programs.

12.7 CONCLUSIONS AND FUTURE PROJECTIONS

12.7.1 Status and Competitiveness of a-Si Photovoltaics

Over the last quarter of a century, significant progress has been made in the understanding of properties and of deposition processes for a-Si-based materials and solar cells. There have been impressive achievements both in increasing the conversion efficiency of solar cells and in reducing the cost of fabrication. In 1997, a-Si-based solar cells with 15.2% initial efficiency and 13% stable efficiency were demonstrated [8]. The manufacturing volume of a-Si solar modules has increased more than tenfold over the past 10 years, and capacity is presently more than 85 MW_p/year. There are now seven a-Si PV manufacturers with production capacity of 2 MW_p/year or more.

In the pipeline for the future, significant progress has been made in the development of rapid deposition processes (>5 Å/s) that achieve essentially the same quality as the present slow processes, as discussed in Section 12.3. As rapid deposition and high gas utilization processes are incorporated into production, further cost reduction will be achieved.

Additionally, the use of microcrystalline silicon as the narrow band gap absorber layer in an a-Si-based tandem solar cell has been demonstrated, and cells exceeding 12% conversion efficiency (stabilized) have been produced in different labs. The cells incorporating μc-Si show superior light stability over extended light soaking.

Amorphous Si-based PV technology is unique compared with other PV technologies. Amorphous Si absorbs sunlight more strongly than c-Si and poly-Si because it is amorphous; the selection rules that weaken absorption in c-Si (an "indirect band gap" semiconductor) do not apply to a-Si. A rather thin layer of a-Si is sufficient to absorb sunlight. Amorphous Si can be made at a low temperature on inexpensive substrates. The product is made through a low-cost process. The energy payback time (the time required for an a-Si module to generate the energy used in its production) was estimated as one to two years in 1989, and has probably shrunk substantially since then [194]. One expects that the cost will continue to decline as the production volume is increased. When deposited on selected substrates, the product can be made lightweight and flexible, which is important for many applications. The output power of a-Si PV products also has a positive temperature coefficient: at higher ambient temperature, for example, in areas with more sunshine, the efficiency is higher.

Compared with other types of thin-film PV technologies, such as CdTe and copper-indium-diselenide (CIS)-based PV technologies that have demonstrated higher efficiency in small-area R&D type cells, a-Si photovoltaics looks attractive because (1) it has been developed for approximately 20 years and the production process is more mature and proven and (2) the product does not contain any hazardous materials such as Cadmium as in CdTe photovoltaics or a large amount of expensive metal such as indium as in CIS-based photovoltaics. The materials in amorphous silicon–based cells originate in raw materials that are abundant on earth.

12.7.2 Critical Issues for Further Enhancement and Future Potential

To increase application of a-Si-based PV significantly beyond today's level, the following issues are critical and must be addressed.

1. Light-induced degradation must be better understood. Approaches for reducing or controlling the degradation need to be further developed. At this moment, there are many engineering compromises in the device design, such as the use of thin i-layers to limit the degradation. If the materials can be made more stable under light, these compromises can be relaxed and the device can be made with much higher efficiency.

2. As the gross defects associated with light soaking are minimized, we shall need to explore improvements in the drift mobility of holes.

3. We need to improve a-SiGe so that narrower band gap materials can be incorporated into cells and more of the infrared region of the solar spectrum can be exploited.

4. Faster deposition processes need to be developed that (at least) preserve the conversion efficiencies achieved by present processes. This is critical for low-cost and high-throughput manufacturing. In addition, these high-rate processes must also achieve high gas utilization.

5. Microcrystalline Si-based solar cells need to be fully explored as alternative, narrow band gap component cells in tandem or triple-junction cells. We expect that rather fast, >20 Å/s, deposition processes will be required. The device physics of μc-Si-based solar cells, especially the possibilities for improving the open-circuit voltage, need to be better understood.

6. Module design needs to be further improved and the costs associated with framing and encapsulation need to be further reduced. At the same time the durability of modules in standard environmental tests must be preserved or improved.

7. We need to find new applications for a-Si PV products in all of its present markets, including building-integrated PV, space power, and consumer electronics as well as grid-connected, large-scale power generation.

As these critical issues are successfully addressed, we expect that a-Si-based solar cells will become more inexpensive, that there will be explosive increases in the volume of production and widespread expansion in the market. Amorphous silicon–based cells will become an environmentally friendly, inexpensive, and a ubiquitous source of electrical power for our life on Earth!

12.8 ACKNOWLEDGMENTS

REFERENCES

1. Williams E, *The Physics and Technology of Xerographic Processes*, Wiley, New York, NY (1984).
2. Mort J, *The Anatomy of Xerography: Its Invention and Evolution*, McFarland, Jefferson, NC (1989).
3. Chittick R, Sterling H, in Adler D, Fritzsche H, Eds, *Tetrahedrally Bonded Amorphous Semi-conductors*, pp. 1–11, Plenum Press, New York, NY (1985).
4. Spear W, LeComber P, *Solid State Commun.* **17**, 1193 (1975).
5. Carlson D, Wronski C, *Appl. Phys. Lett.* **28**, 671 (1976).
6. Perlin J, *Space to Earth: The Story of Solar Electricity*, aatec Publications, Ann Arbor (1999).
7. Wronski C, Carlson D, in Archer M, Hill R, Eds, *Clean Electricity from Photovoltaics*, World Scientific, Singapore (2001).
8. Yang J, Banerjee A, Guha S, *Appl. Phys. Lett.* **70**, 2977 (1997).
9. Fritzsche H, *Mater. Res. Soc. Symp. Proc.* **609**, A17.1.1–12 (2001).
10. Vaněček M Poruba A, Remeš Z, Beck N, Nesládek M, *J. Non-Cryst. Solids* **227–230**, 967 (1998).
11. The figure was calculated based on the hemispherical irradiance (37° south facing) American Society for Testing and Materials (ASTM) Table G159-98 Standard Tables for References Solar Spectral Irradiance at Air Mass 1.5: Direct Normal and Hemispherical for a 37° Tilted Surface.
12. Near room temperature, a-Si:H has a "quantum efficiency" of essentially 1.00 for generating photocarriers when a photon is absorbed. Carasco F, Spear W, *Philos. Mag. B* **47**, 495 (1983). This ideal value is rather surprising. Many other non-crystalline materials have "geminate recombination" of the electron and hole immediately after their generation, which would of course lead to a loss of conversion efficiency; see ref. 13.
13. Schiff E, *J. Non-Cryst. Solids* **190**, 1 (1995).
14. Guha S, in Street R, Ed, *Technology and Applications of Amorphous Silicon*, 252–305, Springer, Berlin (1999). Figure 6.10 of this paper is a valuable compilation of power measurements for varying cell thicknesses and light-soaking histories.
15. Guha S, Yang J, Banerjee A, Glatfelter T, Hoffman K, Xu X, *Technical Digest – 7th International Photovoltaic Science and Engineering Conference (PVSEC-7)*, 43 (Nagoya, Japan, 1993).
16. Staebler D, Wronski C, *Appl. Phys. Lett.* **31**, 292 (1977).
17. Shugar D, *Proc. 24th Photovoltaic Specialists Conference*, 670, IEEE (1994).
18. Measurements furnished through the courtesy of N. Cereghetti, Laboratory of Energy, Ecology and Economy (LEEE), Scuola Universitaria Professionale della Svizzera Italiana. These data apply to the 0.5 kW array, and are described in more detail by Cereghetti N, Chianese D, Rezzonico S, Travaglini G, *Proceedings of the 16th European Photovoltaic Solar Energy Conference*, James & James, London (2001).
19. Emery K, Burdick J, Calyem Y, Dunlavy D, Field H, Kroposki B, Moriary T, Ottoson L, Rummel S, Strand T, Wanlass M, *Proc. 25th Photovoltaic Specialists Conference*, 1275, IEEE (1996).
20. Kameda M, Sakai S, Isomura M, Sayama K, Hishikawa Y, Matsumi S, Haku H, Wakisaka K, Tanaka K, Kiyama S, Tsuda S, Nakano S, *Proc. 25th Photovoltaic Specialists Conference*, 1049, IEEE (1996).
21. del Cueto J, von Roedern B, *Prog. Photovoltaics* **7**, 101 (1999).
22. Carlson D, Lin G, Ganguly G, *Proc. 28th Photovoltaic Specialists Conference*, 707, IEEE (2000).
23. Street R, *Hydrogenated Amorphous Silicon*, Cambridge University Press, Cambridge (1991).
24. Phillips J, *J. Non-Cryst. Solids* **34**, 153 (1979).
25. Boolchand P, Thorpe M, *Phys. Rev. B* **50**, 10366 (1994).

26. Reimer J, Petrich M, in Fritzsche H, Ed, *Amorphous Silicon and Related Materials*, Vol. A, 3–27, World Scientific, Singapore (1989).
27. Zhao Y, Zhang D, Kong G, Pan G, Liao X, *Phys. Rev. Lett.* **74**, 558 (1995).
28. Santos P, Johnson N, Street R, *Phys. Rev. Lett.* **67**, 2686 (1991).
29. Beyer W, Herion J, Wagner H, Zastrow U, *Philos. Mag. B* **63**, 269 (1991).
30. Figure courtesy of R. Biswas; for information on the calculations, see Biswas R, Li Y, *Phys. Rev. Lett.* **82**, 2512 (1999).
31. Jackson W, Tsai C, Thompson R, *Phys. Rev. Lett.* **64**, 56 (1990).
32. Zafar S, Schiff E, *Phys. Rev. Lett.* **66**, 1493 (1991).
33. The assignment of the D-center observed in electron paramagnetic resonance measurements with a dangling bond has been challenged in favor of "floating bonds" (Stathis J, Pantelides S, *Phys. Rev. B* **37**, 6579–6582 (1988)).
34. Park H, Liu J, Wagner S, *Appl. Phys. Lett.* **55**, 2658 (1989).
35. See the review of Fritzsche H, *Annu. Rev. Mater. Res.* **31**, 47 (2001).
36. Branz H, *Phys. Rev. B* **59**, 5498 (1999).
37. Ley L, *J. Non-Cryst. Solids* **114**, 238 (1989).
38. Jackson W, Kelso S, Tsai C, Allen J, Oh S, *Phys. Rev. B* **31**, 5187 (1985).
39. Cody G, Tiedje T, Abeles B, Brooks B, Goldstein Y, *Phys. Rev. Lett.* **47**, 1480 (1981).
40. Tiedje T, in Joannopoulos J, Lucovsky G, Eds, *Hydrogenated Amorphous Silicon II*, 261–300, Springer-Verlag, New York (1984).
41. Gu Q, Wang Q, Schiff E, Li Y, Malone C, *J. Appl. Phys.* **76**, 2310 (1994).
42. Wang Q, Antoniadis H, Schiff E, Guha S, *Phys. Rev. B* **47**, 9435 (1993).
43. Gu Q, Schiff E, Chevrier J, Equer B, *Phys. Rev. B* **52**, 5695 (1995).
44. Mott N, *Conduction in Non-Crystalline Solids*, Oxford University Press, Oxford (1987).
45. Tauc J, in Abeles F, Ed, *Optical Properties of Solids*, 277–313, North Holland, Amsterdam (1972).
46. Chen I, Wronski C, *J. Non-Cryst. Solids* **190**, 58 (1995).
47. Jackson W, Amer N, *Phys. Rev. B* **25**, 5559 (1982).
48. Antoniadis H, Schiff E, *Phys. Rev. B* **46**, 9482–9492 (1992).
49. Lee J, Schiff E, *Phys. Rev. Lett.* **68**, 2972 (1992).
50. Han D, Melcher D, Schiff E, Silver M, *Phys. Rev. B* **48**, 8658 (1993).
51. Hama S, Okamoto H, Hamakawa Y, Matsubara T, *J. Non-Cryst. Solids* **59–60**, 333 (1983).
52. Guha S, Payson J, Agarwal S, Ovshinsky S, *J. Non-Cryst. Solids* **97–98**, 1455 (1987).
53. Middya A, Ray S, Jones S, Williamson D, *J. Appl. Phys.* **78**, 4966 (1995).
54. Stutzmann M, Street R, Tsai C, Boyce J, Ready S, *J. Appl. Phys.* **66**, 569 (1989).
55. Li Y, *Proc. Materials Research Society Symp.*, **297**, 803–814 (1994).
56. Arya R, Catalano A, Oswald R, *Appl. Phys. Lett.* **49**, 1089 (1986).
57. Tsukada T, in Street R, Ed, *Technology and Applications of Amorphous Silicon*, 7–93, Springer, Berlin, Germany (2000).
58. Chittick R, Alexander J, Sterling H, *J. Electrochem. Soc.* **116**, 77–81 (1969).
59. Spear W, LeComber P, *J. Non-Cryst. Solids* **8–10**, 727–738 (1972).
60. Chapman B, *Glow Discharge Processes*, John Wiley & Sons, New York (1980).
61. Luft W, Tsuo Y, *Hydrogenated Amorphous Silicon Alloy Deposition Processes*, Marcel Dekker, New York (1993).
62. Guha S, Yang J, Banerjee A, Glatfelter T, Hoffman K, Ovshinsky S, Izu M, Ovshinsky H, Deng X, *Mater. Res. Soc. Symp. Proc.* **336**, 645 (1994).
63. Arya R, Carlson D, *Prog. Photovoltaics* **10**, 69–76 (2002).
64. Carlson D, US Patent 4,317,844 (1982).
65. Curtins H, Wyrsch N, Shah A, *Electron. Lett.* **23**, 228–230 (1987).
66. Chatham H, Bhat P, Benson A, Matovich C, *J. Non-Cryst. Solids* **115**, 201–203 (1989).
67. Saito K, Sano M, Matsuyama J, Higasikawa M, Ogawa K, Kajita I, *Tech. Digest PVSEC-9*, 579 (1996).

68. Matsumura H, *Jpn. J. Appl. Phys.* **25**, L949–L951 (1986).
69. Mahan A, Carapella J, Nelson B, Crandall R, Balberg I, *J. Appl. Phys.* **69**, 6728–6730 (1991).
70. Konagai M, Kim W, Tasaki H, Hallerdt M, Takahashi K, *AIP Conf. Proc.* **157**, 142–149 (1987).
71. Rocheleau R, Hegedus S, Buchanan W, Jackson S, *Appl. Phys. Lett.* **51**, 133–135 (1987).
72. Paul W, Lewis A, Connel G, Moustakas T, *Solid State Commun.* **20**, 969–972 (1976).
73. Moustakas T, Wronski C, Tiedje T, *Appl. Phys. Lett.* **39**, 721–723 (1981).
74. Knights J, *Mater. Res. Soc. Symp. Proc.* **38**, 372 (1985).
75. Ueda M, Imura T, Osaka Y, *Proc. 10th Symp. on Ion Sources and Ion-Assisted Technology* (1986).
76. Deng X, Narasimhan K, Evans J, Izu M, Ovshinsky S, *Proc. 1st World Conf. on Photovoltaic Energy Conversion*, 678 (1994).
77. Yang J, Xu X, Banerjee A, Guha S, *Proc. 25th Photovoltaic Specialists Conference*, 1041, IEEE (1996).
78. Cherepin V, *Secondary Ion Mass Spectroscopy of Solid Surfaces*, VNW Science Press, Utrecht (1987).
79. Kampas F, *J. Appl. Phys.* **54**, 2276–2280 (1983).
80. Jasinski, J, Whittaker, E, Bjorklunk G, Dreyfus R, Estes R, Walkup R, *Appl. Phys. Lett.* **44**, 1155–1157 (1984).
81. Robertson R, Gallagher A, *J. Chem. Phys.* **85**, 3623–3630 (1986).
82. Gallagher A, *J. Appl. Phys.* **63**, 2406–2413 (1988).
83. Shah A, Dutta J, Wyrsch N, Prasad K, Curtins H, Finger F, Howling A, Hollenstein C, *Mater. Res. Soc. Symp. Proc.* **258**, 15 (1992).
84. Heintze M, Zedlitz R, Bauer G, *Mater. Res. Soc. Symp. Proc.* **297**, 49–54 (1993).
85. Deng X, Jones S, Liu T, Izu M, Ovshinsky S, *Proc. 26th Photovoltaic Specialists Conference*, 591, IEEE (1997).
86. Ito N, Kondo M, Matsuda A, *Proc. 28th Photovoltaic Specialists Conference*, 900 (2000).
87. Kato I, Wakana S, Hara S, Kezuka H, *Jpn. J. Appl. Phys.* **21**, L470 (1982).
88. Hudges S, Johncock A, Ovshinsky S, *J. Non-Cryst. Solids* **77–78**, 809 (1985).
89. Watanabe T, Azuma K, Nakatani M, Suzuki K, Sonobe T, Shimada T, *Jpn. J. Appl. Phys.* **25**, 1805 (1986).
90. Guha S, Xu X, Yang J, Banerjee A, *Appl. Phys. Lett.* **66**, 595–597 (1995).
91. Saito K, Sano M, Ogawa K, Kajita I, *J. Non-Cryst. Solids* **164–166**, 689 (1993).
92. Saito K, Sano M, Matsuyama J, Higasikawa M, Ogawa K, Kajita I, *Tech. Digest PVSEC-9*, 579 (1996).
93. Wiesmann H, Ghosh A, McMahon T, Strongin M, *J. Appl. Phys.* **50**, 3752 (1979).
94. Wang Q *et al.*, *Proc. 29th Photovoltaic Specialists Conference*, 1222–1225, IEEE (2002).
95. Wang Q, Iwaniczko E, Yang J, Lord K, Guha S, Wang K, Han D, *J. Non-Cryst. Solids* **299–302**, 2–8 (2002).
96. Mahan A, Xu Y, Nelson B, Crandall R, Cohen J, Palinginis K, Gallagher A, *Appl. Phys. Lett.* **78**, 3788 (2001).
97. Povolny H, Deng X, to be published in *Thin Solid Films* (2003).
98. Morrison S, Madan A, *Proc. 28th Photovoltaic Specialists Conference*, 837, IEEE (2000).
99. Moustakas T, Maruska H, Friedman R, *J. Appl. Phys.* **58**, 983–986 (1985).
100. Abelson J, Doyle J, Mandrell L, Maley N, *Mater. Res. Soc. Symp. Proc.* **268**, 83–94 (1992).
101. Miller D, Lutz H, Weismann H, Rock E, Ghosh A, Ramamoorthy S, Strongin M, *J. Appl. Phys.* **49**, 6192, 6193 (1978).
102. Shimizu T, Kumeda M, Morimoto A, Tsujimura Y, *Mater. Res. Soc. Symp. Proc.* **70**, 311–318 (1986).
103. Hanna J, Kamo A, Azuma M, Shibata N, Shirai H, Shimizu I, *Mater. Res. Soc. Symp. Proc.* Vol. 118, 79–84 (1988).
104. Parsons G, Tsu D, Lucovsky G, *J. Vac. Sci. Technol., A* **6**, 1912–1916 (1988).

105. Sakamoto Y, *Jpn. J. Appl. Phys.* **16**, 1993–1998 (1977).
106. Dalal V, Maxson T, Girvan R, Haroon S, *Mater. Res. Soc. Symp. Proc.* **467**, 813–817 (1997).
107. Hanabusa M, Suzuki M, *Appl. Phys. Lett.* **39**, 431, 432 (1981).
108. Ovshinsky S, Deng X, Young R, US Patent 5,231,047 (1993).
109. Jones S, Crucet R, Deng X, Izu M, *Mater. Res. Soc. Symp. Proc.* **609**, A4.5 (2000).
110. Guha S, Narasimhan K, Pietruszko S, *J. Appl. Phys.* **52**, 859 (1981).
111. Tanaka K, Matsuda A, *Mater. Sci. Rep.* **2**, 139–184 (1987).
112. Yang J, Lord K, Guha S, Ovshinsky S, *Mater. Res. Soc. Symp. Proc.* **609**, A15.4 (2000).
113. Yang J, Xu X, Guha S, *Mater. Res. Soc. Symp. Proc.* **336**, 687–692 (1994).
114. Yang L, Chen L, *Mater. Res. Soc. Symp. Proc.* **336**, 669–674 (1994).
115. Ferlauto A, Koval R, Wronski C, Collins R, *Appl. Phys. Lett.* **80**, 2666 (2002).
116. Yang J, Banerjee A, Lord K, Guha S, *Proc. 28th Photovoltaic Specialists Conference*, 742, IEEE (2000).
117. Deng X, *Record of the NREL-EPRI Amorphous Silicon Guidance Team Review Meeting* (Feb. 25–26, 2002).
118. Deng X, *Development of High, Stable-Efficiency Triple-Junction a-Si Alloy Solar Cells*, Annual Subcontract Report, Submitted to NREL, NREL/TP-411-20687, Feb. 1996.
119. Ovshinsky S, Guha S, Yang C, Deng X, Jones S, US Patent 8,766,219 (1996).
120. Liao X, Wang W, Deng X, *Proc. 29th Photovoltaic Specialists Conference*, 1234–1237, IEEE (2002).
121. Koval R, Chen C, Gerreira G, Ferlauto A, Pearce J, Rovira P, Collins R, Wronski C, *Proc. 29th Photovoltaic Specialists Conference*, 1090–1093 (2002).
122. AMPS-1D is a copyright of Pennsylvania State University. Zhu H, Fonash S, *Symp. Proc.*, Vol. 507, 395–402 (1998).
123. Schropp R, Zeman M, *Amorphous and Microcrystalline Silicon Solar Cells: Modeling Materials, and Device Technology*, Kluwer, Boston, MA (1998).
124. Welcome, expert. The electronic characteristics of a-Si:H used in the modeling in this chapter include only bandtail states – and not defects. The parameters for a-Si:H are published in Jiang L, Rane S, Schiff E, Wang Q, Yuan Q, *Symp. Proc.*, Vol. 609, A18.3.1–A18.3.11 (2001).
125. $K = \{\sin(\alpha\pi)\}/\{\alpha(1 - \alpha)\pi\}$.
126. Scher H, Shlesinger M, Bendler J, *Phys. Today* **44**, 26 (1991).
127. Crandall R, *J. Appl. Phys.* **54**, 7176 (1983).
128. Hegedus S, *Prog. Photovoltaics* **5**, 151 (1997).
129. Crandall R, Schiff E, in Ullal H, Witt C, Eds, *13th NREL Photovoltaics Program Review*, *Conf. Proc.*, Vol. 353, 101–106, American Institute of Physics, Woodbury (1996).
130. Pearce J, Koval R, Ferlauto A, Collins R, Wronski C, Yang J, Guha S, *Appl. Phys. Lett.* **77**, 19 (2000).
131. Rose A, *Photoconductivity and Allied Phenomena*, Robert E. Krieger, Huntington, NY (1978).
132. Fonash S, *Solar Cell Device Physics*, John Wiley & Sons, New York, NY (1981).
133. Tiedje T, *Appl. Phys. Lett.* **40**, 627 (1982).
134. Guha S, Yang J, Nath P, Hack M, *Appl. Phys. Lett.* **49**, 218 (1986).
135. Arya R, Catalano A, Oswald R, *Appl. Phys. Lett.* **49**, 1089 (1986).
136. Hegedus S, Rocheleau R, Tullman R, Albright D, Saxena N, Buchanan W, Schubert K, and Dozler R, *Conference Record of the 20th IEEE Photovoltaic Specialists Conference*, 129–134, IEEE (1988).
137. Hegedus S, Rocheleau R, Tullman R, Albright D, Saxena N, Buchanan W, Schubert K, Dozler R, *J. Appl. Phys.* **67**, 3494 (1990).
138. Hegedus S, Deng X, *Conference Record of the 25th IEEE Photovoltaic Specialists Conference*, 1061–1064, IEEE (1996).
139. Yablonovitch E, *J. Opt. Soc. Am.* **72**, 899 (1982).
140. Deckman H, Wronski C, Witzke H, Yablonovitch E, *Appl. Phys. Lett.* **42**, 968 (1983).

141. Hegedus S, Buchanan W, Liu X, Gordon R, *Conference Record of the 25th IEEE Photovoltaic Specialists Conference*, 1129−1132, IEEE (1996).
142. Lechner P, Geyer R, Schade H, Rech B, Müller J, *Conference Record of the 28th IEEE Photovoltaic Specialists Conference*, 861−864, IEEE (2000).
143. Banerjee A, Guha S, *J. Appl. Phys.* **69**, 1030 (1991).
144. Sze S, *Physics of Semiconductor Devices*, 798, John Wiley & Sons, New York, NY (1981)
145. Mitchell K, *Tech. Digest 1st International Photovoltaic Solar Energy Conversion*, 691−694 (1984).
146. Kuwano Y *et al.*, *Conference Record of the 16th IEEE Photovoltaic Specialists Conference*, 1338−1343, IEEE (1982).
147. The thickness of i-layers are in the range of 100 nm to 200 nm, while for single junction a-Si solar cells the i-layer needs to be much thicker to get high efficiency.
148. Hack M, Shur M, *J. Appl. Phys.* **59**, 2222 (1986).
149. Agarwal P, Povolny H, Han S, Deng X, *J. Non-Cryst. Solids* **299-302**, 1213−1218 (2002).
150. Meier J, Fluckiger R, Keppner H, Shah A, *Appl. Phys. Lett.* **65**, 860−862 (1994).
151. Yang L, Chen L, Catalano A, *Mater. Res. Soc. Symp. Proc.* **219**, 259−264 (1991).
152. Guha S, Yang J, Pawlikiewicz A, Glatfelter T, Ross R, Ovshinsky S, *Appl. Phys. Lett.* **54**, 2330 (1989).
153. Zimmer J, Stiebig H, Wagner H, *J. Appl. Phys.* **84**, 611−617 (1998).
154. Yang J, Banerjii, A, Glatfelter T, Sugiyama S, Guha S, *Conference Record of the 26th IEEE Photovoltaic Specialists Conference*, 563−568, IEEE (1997).
155. Hamakawa Y, Tawada Y, Nishimura K, Tsuge K, Kondo M, Fujimoto K, Nonomura S, Okamoto H, *Conference Record of the 16th IEEE Photovoltaic Specialists Conference*, 679−684, IEEE (1982).
156. Guha S, in Street R, Ed, *Technology and Applications of Amorphous Silicon*, Springer-Verlag, Berlin, Heidelberg, New York (2000). (See Table 6.9 in the reference.)
157. Yoshida T, Tabuchi K, Takano A, Tanda M, Sasaki T, Sato H, Fijikake S, Ichikawa Y, Harashima K, *Conference Record of the 28th IEEE Photovoltaic Specialists Conference*, 762−765 (2000).
158. Wang W, Povolny H, Du W, Liao X, Deng X, *Conference Record of the 29th IEEE Photovoltaic Specialists Conference*, 1082−1085 (2002).
159. Nomoto K, Saitoh H, Chida A, Sannomiya H, Itoh M, Yamamoto Y, *Intl. Tech. Digest PVSEC-7*, 275 (1993).
160. Arya R, Oswald R, Li Y, Maley N, Jansen K, Yang L, Chen L, Willing F, Bennett M, Morris J, Carlson D, *Proc. 1st World Conf. Photovoltaic Solar Energy Conversion*, 394 (1994).
161. Hishikawa Y, Ninomiya K, Maryyama E, Kuroda S, Terakawa A, Sayama K, Tarui H, Sasaki M, Tsuda S, Nakano S, *Proc. 1st World Conf. Photovoltaic Solar Energy Conversion*, 386−393 (1994).
162. Meier J, Keppner H, Dubail S, Droll U, Torres P, Pernet P, Ziegler Y, Selvan J, Cuperus J, Fischer D, Shah A, *Mater. Res. Soc. Symp. Proc.* **507**, 139−144 (1998).
163. Saito K, Sano M, Matuda K, Kondo Takaharu, Nishimoto T, Ogawa K, Kajita I, *Proc. 2nd World Conf. Photovoltaic Solar Energy Conversion*, 351−354 (1998).
164. Yamamoto K, Yoshimi M, Suzuki T, Okamoto Y, Tawada Y, Nakajima A, *Conference Record of the 26th IEEE Photovoltaic Specialists Conference*, 575−580 (1997).
165. Jones S, Crucet R, Capangpangan R, Izu M, Banerjee A, *Mater. Res. Soc. Symp. Proc.* **664**, A15.1 (2001).
166. Yang J, Banerjee A, Lord K, Guha S, *Proc. 2nd World Conf. on Photovoltaic Energy Conversion*, 387−390 (1998).
167. Iida H, Shiba N, Mishuka T, Karasawa H, Ito A, Yamanaka M, Hayashi Y, *IEEE Electron Device Lett.* **EDL-4**, 157−159 (1983).
168. Gordon R, Proscia J, Ellis F, Delahoy A, *Sol. Energy Mater.* **18**, 263−281 (1989).
169. Hegedus S, Kampas F, Xi J, *Appl. Phys. Lett.* **67**, 813 (1995).

170. Burdick J, Glatfelter T, *Sol. Cells* **18**, 310–314 (1986).
171. Mueller R, *Sol. Energy Mater. Sol. Cells* **30**, 37–45 (1993).
172. Veprek S, Marecek V, *Solid-State Electron.* **11**, 683 (1968).
173. Hattori Y, Kruangam D, Toyama T, Okamoto H, Hamakawa Y, *Tech. Digest PVSEC-3*, 171 (1987).
174. Faraji M, Gokhale S, Ghoudhari S, Takwake M, Ghaisas S, *Appl. Phys. Lett.* **60**, 3289–3291 (1992).
175. Meier J, Kroll U, Dubail S, Golay S, Fay S, Dubail J, Shah A, *Conference Record of the 28th IEEE Photovoltaic Specialists Conference*, 746–749 (2000).
176. Yamamoto K, *Mater. Res. Soc. Symp. Proc.* **507**, 131–138 (1998).
177. Repmann T, Appenzeller W, Roschek T, Rech B, Wagner H, *Conference Record of the 28th IEEE Photovoltaic Specialists Conference*, 912–915 (2000).
178. Rath J, Galetto M, van der Werf C, Feenstra K, Meiling H, van Cleef M, Schropp R, *Tech. Dig. 9th Int. PV Sci. and Eng. Conf.*, 227 (1996).
179. Jones S, Crucet R, Deng X, Izu M, *Mater. Res. Soc. Symp. Proc.* **609**, A4.5 (2000).
180. Roschek T, Repmann T, Muller J, Rech B, Wagner H *et al.*, *Conference Record of the 28th IEEE Photovoltaic Specialists Conference-1996*, 150–153 (2000).
181. Meier J, Dubail S, Cuperus J, Kroll U, Platz R, Torres P, AnnaSelvan J, Pernet P, Pellaton N, Fischer D, Keppner H, Shah A, *J. Non-Cryst. Solids* **227–230**, 1250 (1998).
182. Platz R, Pellaton Vaucher N, Fischer D, Meier J, Shah A, *Conference Record of the 26th IEEE Photovoltaic Specialists Conference*, 691–694 (1997).
183. Shah A, Meier J, Vallat-Sauvain E, Droz C, Kroll U, Wyrsch N, Guillet J, Graf U, *Thin Solid Films* **403–404**, 179–187 (2002).
184. Izu M, Ovshinsky S, *Thin Solid Films* **119**, 55 (1984).
185. Izu M, Deng X, Krisko A, Whelan K, Young R, Ovshinsky H, Narasimhan K, Ovshinsky S, *Conference Record of the 23th IEEE Photovoltaic Specialists Conference*, 919 (1993).
186. Banerjee A, Yang J, Guha S, *Mater. Res. Soc. Symp. Proc.* (1999).
187. Deng X, Narasimhan K, *IEEE 1st World Conf. on Photovoltaic Energy Conversion*, 555 (1994).
188. Nath P, Hoffman K, Vogeli C, Ovshinsky S, *Appl. Phys. Lett.* **53**, 986–988 (1988).
189. Frammelsberger W, Lechner P, Rubel H, Schade H, *Proc. 14th European Photovoltaic Solar Energy Conference*, 2006 (1997).
190. Forest H, *Proc. 14th European Photovoltaics Solar Energy Conf.*, 2018–2020 (1997).
191. Rech B *et al.*, *Proc. 2nd World Conf. on Photovoltaic Solar Energy Conversion*, 391–396 (1998).
192. Kinoshita T *et al.*, *Proc. 14th EU Photovoltaic Solar Energy Conversion*, 566 (1997).
193. Okamoto S, Terakawa A, Maruyama E, Shinohara W, Hishikawa Y, Kiyama S, *Conference Record of the 28th IEEE Photovoltaic Specialists Conference*, 736–741 (2000).
194. Hagedorn G, *Proc. 9th European Photovoltaic Solar Energy Conversion*, 542 (Freiburg, 1989).
195. Yamamoto K, Yoshimi M, Suzuki T, Nakata T, Swada T, Nakajima A, Hayashi K, *Conference Record of the 28th IEEE Photovoltaic Specialists Conference*, 1428–1432 (2000).